Published in final edited form as:

MAGMA. 2016 June ; 29(3): 617–639. doi:10.1007/s10334-016-0561-4.

Toward 20 T magnetic resonance for human brain studies: opportunities for discovery and neuroscience rationale

Thomas F. Budinger[1], **Mark D. Bird**[2], **Lucio Frydman**[2,3], **Joanna R. Long**[4], **Thomas H. Mareci**[4], **William D. Rooney**[5], **Bruce Rosen**[6], **John F. Schenck**[7], **Victor D. Schepkin**[2], **A. Dean Sherry**[8], **Daniel K. Sodickson**[9], **Charles S. Springer**[5], **Keith R. Thulborn**[11], **Kamil Uğurbil**[10], and **Lawrence L. Wald**[6]

[1]Lawrence Berkeley National Laboratory, University of California, Berkeley, CA, USA

[2]National High Magnetic Field Laboratory, Florida State University, Tallahassee, FL, USA

[3]Weizmann Institute, Rehovot, Israel

[4]McKnight Brain Institute, University of Florida, Gainesville, FL, USA

[5]Oregon Health and Sciences University, Portland, OR, USA

[6]Massachusetts General Hospital, Harvard Medical School, Harvard, MA, USA

[7]General Electric Corporate Research, Schenectady, NY, USA

[8]University of Texas Southwestern Medical Center, Dallas, TX, USA

[9]School of Medicine, New York University, New York, NY, USA

[10]University of Minnesota, Minneapolis, MN, USA

[11]University of Illinois, Chicago, IL, USA

Abstract

An initiative to design and build magnetic resonance imaging (MRI) and spectroscopy (MRS) instruments at 14 T and beyond to 20 T has been underway since 2012. This initiative has been supported by 22 interested participants from the USA and Europe, of which 15 are authors of this review. Advances in high temperature superconductor materials, advances in cryocooling engineering, prospects for non-persistent mode stable magnets, and experiences gained from large-bore, high-field magnet engineering for the nuclear fusion endeavors support the feasibility of a human brain MRI and MRS system with 1 ppm homogeneity over at least a 16-cm diameter volume and a bore size of 68 cm. Twelve neuroscience opportunities are presented as well as an analysis of the biophysical and physiological effects to be investigated before exposing human subjects to the high fields of 14 T and beyond.

Correspondence to: Thomas F. Budinger.

Compliance with ethical standards

Conflict of interest The authors declare that they have no conflicts of interest.

Keywords

Magnetic resonance imaging; Ultrahigh magnetic fields; High temperature superconductors; Diffusion tensor imaging; Parallel transmit and receive strategies; Human brain chemistry; Magnetic field physiologic effects

Introduction

The full potential of magnetic resonance imaging and spectroscopy (MRI and MRS) to reveal the hitherto unknown functional patterns and biochemistry of the normal and dysfunctional human brain have not been realized due to the limited sensitivity and hence spatial and spectral resolution of the MR technique, as well as the limited performance of gradient and radiofrequency (RF) coils. These limitations can be overcome by developing magnets with field-strengths beyond those currently available (i.e., 14–20 T) and improvements in the performance of associated gradient and RF coils. We anticipate that at magnetic fields at and above 14 T, in vivo measurements at resolutions of less than 100 μm will be feasible on timescales compatible with human tolerances. Modeling and experimental studies show that the required timing and resolution for imaging computational elements of the brain require higher magnetic fields than those currently available (Fig. 1). The highest resolution for the human brain achieved at 7 T is 0.2 mm isotropic using prospective motion compensation and lengthy averaging. Isotropic resolution of 0.65 mm has been achieved for function MRI (fMRI). Reduction of the voxel volume to 0.1 μL or less provides unprecedented biologically relevant resolution gains in a spatially non-homogeneous and curved structure such as the brain. It allows, for example, resolution of the six layers defined by the neuron types across the cortical thickness, and ~2 voxels across a column on the cortical surface, using isotropic voxel dimensions. It will also allow semi-quantitative mapping of the distribution of aggregated proteins (e.g., amyloid plaques and phosphorylated Tau protein) through susceptibility anisotropy.

If we assume the signal-to-noise ratio (SNR) scales linearly or better with a magnetic field in the human brain, as it has been shown for up to 9.4 T [1] and linearly with fields from 9.4 to 21.1 T (vide infra), magnetic fields of 14 T and above will provide significant gains towards the goal of 0.1-μL volume resolution. If we consider the BOLD (blood oxygen level-dependent) effect to increase at least linearly with magnetic field magnitude [2], then the combined effects of SNR and BOLD contrast would translate into a quadratic gain with field magnitude or ~eightfold gain in contrast-to-noise ratio for functional mapping signals that define the ultimate resolution of the functional maps.

The Human Connectome Project focused on the development of MR methods to measure long-range structural connectivity at 3 and 7 T [3] and defined the foundational methods for mapping brain connectivity. However, the fidelity of the derived structural connectivity is limited by the SNR. Ultrahigh-field magnet development providing important gains in SNR [4], research on optimizing gradient performance [5], and the new innovations in RF and shim coil design shown in this paper promise to make transformative changes in approaches to functional brain imaging.

Ultrahigh fields open unique doors to the interrogation of individual brain metabolites. Neurotransmitters such as glutamine, glutamate, and GABA can easily be distinguished from energetic reporters such as lactate, glucose, and ATP. Also, heteronuclear MRS and MRSI measurements using stable ^{13}C and ^{17}O tracers and naturally abundant ^{31}P can enable brain function maps of energetics not available to studies even at 7 T. The sensitivity boost arising from ≥14 T fields will lead to ^{23}Na, ^{35}Cl, ^{39}K, and possibly other nuclide mapping at unprecedented spatial resolutions and signal strengths.

In this paper we first present the recent developments in enabling technologies: high-field magnets, RF transmit and receive coil array innovation, and gradient coil development directions. Then we review 12 scientific horizons, many of which are or can be demonstrated in animal studies at currently available MRI/MRS magnets at fields up to 21.1 T. Lastly, we present analyses of physiological effects and potential safety issues relevant to human subject MRI and MRS experiments at fields of 9.4 to 20 T.

Advances in technologies that enable >14–20 T MRI

Magnet technology

Human head and whole-body MRI magnets developed to date operate at less than 12 T and use NbTi as the superconducting element (Fig. 1). Moving beyond 11.7 T will require conductors that can carry supercurrent at higher fields such as Nb_3Sn and high-temperature superconductor (HTS)-based conductors relying on either ReBCO, Bi2212, or Bi2223 superconductor materials (Re refers to a rare-earth element, typically Y or Gd) (Fig. 2).

For magnets in the 12–16 T range, Nb_3Sn would be the material of choice for the innermost (high-field) coils. This wire is presently used in persistent small-bore NMR spectrometer magnets up to 23.5 T built by Bruker in Germany, and in large, high-field magnets providing fields up to 13 T in a 50-cm warm-bore [6] and 11.3 T (on-axis) in a 158-cm cold-bore [7]. As seen in Fig. 2 above, the current–density of NbTi at 7 T is ~700 A/mm^2, while the current–density of Nb_3Sn at 14 T is >1000 A/mm^2. This suggests that a future 14 T Nb_3Sn-based magnet may have a similar amount of superconductor in it as that required for a 7 T NbTi-based magnet today. However, the Lorenz forces acting on the conductor are given by $j \times B$ (product of current–density and magnetic field). Thus, the hoop stress in the 14 T coil will be approximately twice that of the 7 T coil. Today's MRI magnets use copper reinforcement [8, 9]. The large, high-field magnets mentioned above use steel reinforcement, which has five times the strength and twice the stiffness of copper. Consequently, by using Nb_3Sn instead of NbTi and steel reinforcement instead of copper, a 14 T human MRI magnet should actually be smaller than the largest MRI magnet in development today [10].

Presently, ultrahigh-field magnets for condensed matter physics [11] and NMR [12] use multiple nested coils. This allows Nb_3Sn to be used for the high-field regime while less expensive NbTi is used for the low-field regime (<10 T). In addition, the nested coil strategy allows different ratios of copper to superconductor to be used for different sections of the magnet, and it also allows for reduction of the hoop-stress in the inner coils [13]. Human MRI magnets above 3 T already use multiple nested coils [8]. As we continue to push MRI beyond 12 T, it will become appropriate to use Nb_3Sn for the inner coils and NbTi for the

outer ones. When we reach ~17 T it will likely become appropriate to use high-temperature superconductors (HTS) for the innermost coils.

At fields >17 T, HTS materials carry higher current-densities and will result in more compact magnets, which should also reduce the cost of the magnet compared with one relying only on the low-temperature superconductor (LTS) materials. While HTS materials have been known since 1986, limitations in strength, current density, and manufacturing processes precluded their use in ultrahigh-field magnets. Three new conductors have emerged in recent years (2007 SuperPower YBCO tape with 600 MPa strength [14], 2012 NHMFL over-pressure-processed isotropic Bi2212 [15], and 2014 Sumitomo Ni–Cr-reinforced Bi2223 [16]). The incorporation of HTS materials with LTS materials into actively stabilized LTS/HTS duplex designs operating in non-persistent mode promises to open the possibility of human MRI magnets at fields >16 T. For example, two all-superconducting magnets generating fields of 26 and 27 T were demonstrated in 2015. A 32 T all-superconducting magnet is being constructed by the National High Magnetic Field Laboratory (NHMFL). The design is a combination of five LTS coils with two HTS coils in a concentric assembly [17]. It will be completed for users at NHMFL in 2016.

A high-field magnetic resonance instrument operating in the non-persistent mode was first demonstrated in a 600-MHz (14.1 T) NMR magnet based on Nb_3Sn tape built by Intermagnetics General Corporation for Carnegie-Mellon University in the late 1970s and was more recently re-introduced by the Japanese ultrahigh-field NMR effort in 2009 utilizing LTS and HTS coils at 9.4 and 2.3 T, respectively, running in an ultrastabilized mode that delivered a conventional set of 500 MHz (11.7 T) high-resolution biomolecular NMR spectra despite running non-persistently [18]. In 2015 the Japanese group has reached 1020 MHz (23.9 T) with a similar test-coil system [19]. While these are magnets for NMR spectroscopy studies with narrow bores, they embody a proof of concept that gives confidence that MRI magnets at 16 T and beyond can be built to operate in the non-persistent mode.

By incorporating HTS materials and coils, fields exceeding 20 T are possible with a volume suitable for human MRI. The advancements that enable this expectation are: (1) improvements in HTS material performance and reliability; (2) development of magnet technologies using HTS materials at the National High Magnetic Field Laboratory and elsewhere with demonstrated fields over 40 T; and (3) demonstrated use of non-persistent mode operation until the reliability of HTS persistent joints is achieved. Development is still needed to meet the stability and uniformity requirements of MRI. The physiological and human-safety aspects of high magnetic fields are discussed under that section of this paper.

Large magnets typically use cables instead of single strands of wire. This results in a magnet of higher current and lower inductance, which simplifies protecting the magnet if a quench occurs. To date, all human MRI magnets have used the single-strand approach. The “Iseult” magnet is an 11.7 T MRI magnet being developed as a joint French-German collaboration [9]. This magnet will be the first human MRI magnet to employ a NbTi cable. As we continue to move into the large-magnet regime to reach higher fields for MRI, Nb_3Sn and HTS cables will be used. While Nb_3Sn cables have been used extensively for high-field

condensed-matter physics, fusion, and for accelerator magnets, HTS cables suitable for use at high fields are in their infancy. This is a very active field of research at present with various HTS materials (YBCO, Bi2212, Bi2223) being cabled in a number of configurations in the pursuit of ultrahigh-field large magnets. At present, the accelerator community has been leading the development of Conductor on Round Core using YBCO tape [20] and the Rutherford cable based on Bi2212 round-wire [21]. The fusion community has championed twisted stacks of YBCO tape [22]. It is too early to say which technology will be best suited for MRI in the 17–21 T range.

Gradient coils for ultrahigh fields at 14–20 T

Magnetic field gradients are of primary importance for spatial/spectral resolution in functional, spectroscopic, and anatomical MRI experiments. Additionally, the potentials for high spatial resolution neuronal fiber architectural studies of the human brain with diffusion-weighted MRI depend on the improvements in gradient coils and pulse sequences that allow safe operations relative to peripheral nerve stimulation (PNS).

Lorentz forces and coupling challenges associated with the DC field, magnet bore volume, and gradient magnitude as well as acoustic noise are the engineering challenges specific to ultrahigh-field operation [23, 24]. Gradients in 7 T systems already operate at higher maximal gradient strengths than those available on clinical scanners but not as high as what is achieved in the two “Connectome” systems, which achieve 300 mT/m (Massachusetts General Hospital instrument) and 100 mT/m (Washington University/University of Minnesota instrument). Though such “Con-nectome” level maximal gradient strengths are not commercially available for 7 T at the present, there is no reason that they cannot be put in a 7 T system, as the mechanical engineering issues can be solved. If the forces that threaten the magnet components or the acoustic noise are beyond regulatory limits, those gradient coils can be operated at 150 mT/m at 7 T for example, thus approximately mimicking the forces encountered at 3 T using 300 mT/m. The observation that the 300 mT/m 3 T Connectome gradient is acoustically quieter than clinical scanners suggests that the thicker, heavier gradient tube needed to support the larger gradient fields can help mitigate the acoustic noise needs. A further approach to meeting the challenge for high-performance gradients at high fields would be based on matrices of gradient coils and use of associated non-linear gradient encoding reconstruction algorithms [25].

To realize the opportunities for neuronal fiber tracking due to the increase in SNR with significantly higher fields than 7 T, development of gradients well beyond 70 mT/m will be necessary. For brain studies these can be head gradients. Evidence given below shows that fiber tract identification in the 0.22-mm range can be achieved based on experiments by one of the authors (TM) at the University of Florida 17.6 magnet using a gradient of 364 mT/m. This high maximal gradient strength is necessary to keep the TE short in diffusion imaging to compensate for the shorter T^*_2 and T_2 decays as the field increases. Faster slew rates also help to shorten the EPI readout, making the images less affected by susceptibility gradients, and allow shorter TE. The slew rate of current gradient designs for the whole body are essentially limited from the well-known PNS thresholds from induced E-fields (vide infra Induced Electric Potentials). Future increases in gradient strength and slew rate for human

gradients will therefore only be possible if PNS and cardiac stimulation thresholds are explicitly taken into account as design criteria.

Human subjects have been exposed to diamagnetic forces of 85 T^2 m^{-1} (force/volume = $\chi/\mu_0 \times B \times dB/dz$ in units of Nm^{-3}). Common commercially available head gradients have improved PNS thresholds (since the shoulders and torso are not stimulated) and can provide maximum gradient amplitudes of 100 mT/m at slew rates well above 400 T/m/s. However, with a focus on the brain, the FOV is reduced to ~20 cm, thus reducing the region where gradients need to be linear. A second approach is to design the gradient fields themselves to minimize body current flows. As the induced E-fields are proportional to the effective current loop diameter, slew rates can be increased substantially for human brain imaging. This will enable the higher performance gradients such as those needed to realize the advantages of high fields in diffusion MRI (DWI) and tractography. These will require investigations of interactions with main magnetic field and noise minimization engineering.

Shim coil array approach—The Massachusetts General Hospital Group [26] and the Duke University Group [27] have independently developed an innovative solution to the age-old shimming problem by increasing the spatial degrees of freedom present in the shim array and integrating the role of the receive RF array and the matrix shim array so that each array is optimally placed close to the body. Successful implementation of this arrangement provides spatial Rx information for parallel imaging acceleration and efficient high-order spatial B_0 shim coils.

Preliminary tests (Fig. 3) show that the dual-purpose loops can function efficiently as both shim coils and RF receiver coils without compromising the performance of either system. Our preliminary experimental tests of individual loop coils have shown this. We have validated this approach at 3 T with a 32-channel combined RF shim-coil array [28]. The low inductance loops can meet the requirements for dynamic shimming using low-voltage amplifiers. The 2nd through 6th order shims are compared to the matrix shim approach. A 64-channel brain matrix RF-shim array using a maximum of 3 A of current in any single loop is comparable to a full set of 1st–5th order shim coils and can substantially improve the B_0 shim at 7 T

Transmit/receive (*T*x/*R*x) coils for 14–20 T MRI/S

The introduction of circular polarized RF transmission coils and arrays [29] and the demonstration of human brain imaging at 400 MHz (9.4 T) [30] have shown that previously considered limitations for ultrahigh magnetic field MRI due to dielectric properties of the brain can be overcome. Multiple coil approaches using independently adjustable elements can improve the homogeneity of the B_1 field [31], and methods to accommodate increased chemical shift dispersion [32] have continued to improve the performance of ^1H imaging at high magnetic fields. This suggests that a new class of experimental techniques may be developed by exploiting the quasioptical nature of RF at these frequencies.

Transmit/receive (*T*x/*R*x) coil arrays have become a principal tool for making high-quality MR images at high fields. Array *R*x performance is expected to be critical for functional MRI at 14 T and above, and array *T*x is expected to be critical for producing uniform tip-

angle distributions in the high dielectric environment of the brain. Performance is known to improve with frequency [33].

For 14–20 T human brain studies, a potential design is a loop size of ~5 cm in a 64–128 channel *R*x array using a capacitance loop element design that is tuned and matched for 600 MHz (14 T). On the parallel transmission (pTx) side, this function can be used to minimize both global and local specific absorbance rates (SAR) [34]. A candidate for array *T*x at 14–20 T is the electric dipole element. Radiation is efficient as the dimensions approach a half-wavelength, and 5 cm is ideally sized for 14–20 T where the wavelength in tissue is ~7 and 5 cm at 600 and 850 MHz frequencies, respectively.

Currently, commercial systems are available for a two-channel pTx. The Siemens system allows full pTx operation (separate waveforms to each channel) and manages the SAR in an FDA-approved manner, by checking local SAR in advance in multiple body models and monitoring waveforms in real time.

Expansion of commercial pTx to more channels has been limited for a number of reasons, including SAR management, ease of use, and extent of impact on driving clinical applications at comparatively low field strengths. However, techniques for SAR and temperature prediction/monitoring continue to advance, and regulatory shifts emphasizing temperature dose over SAR per se may enable more rational (if more difficult to compute) safety thresholds. Meanwhile, it should be noted that pTx at ultrahigh field (UHF) provides additional degrees of freedom that can in fact allow SAR control and even reduction [34, 35]. Safety with respect to component failures is ensured by monitoring the forward and reflected power for each channel in real time and comparing to expectations, as is done in the two-channel Siemens system. If a component fails, causing a change in coil impedance, the system detects it as a sudden change in, say, reflected power, and shuts down. Finally, regarding workflow challenges, new approaches to multicoil high-field transmission have recently been demonstrated, in which excitations are interleaved among coils or coil combinations rather than being played out truly in parallel. Such approaches include the time-interleaved acquisition of modes technique [36] and the new plug-and-play pTx approach using MR Fingerprinting [37]. These approaches have the potential to reduce SAR significantly, in exchange for modifications of the acquisition sequence. In summary, there are many reasons to expect that multicoil transmission will enable robust and safe signal excitation at field strengths substantially higher than those used routinely today.

RF transmit dipole phased array—In a series of simulations with various antenna array designs, the Berlin UHF group [38] showed remarkable uniformity of B_1, and major reductions in SAR can be expected for fields to 20 T and beyond using their phased array design and pulse sequences. Phased array electric dipole antennas with their small dimension in the axial plane and improved decoupling allow at least 20 transmit channels around the human head. The result is an improved spread of RF power over the surface while constructive summation of each propagated wave increases B1+ in the center of the human head. Equally important is the drastic reduction in predicted specific absorbed power (SAR). The SAR increase for 23 T relative to 7 T was only a factor of 1.8.

Human subject motion compensation—The need for subject motion compensation becomes much more of an issue at high fields where higher resolution imaging is a major goal. The motion of the brain and head can be compensated by optical tracking methods. These have yielded major reductions in the blurring from head motion, especially in long scans [39, 40]. Transmitted momenta from cardiac and respiratory functions result in pulsations whose amplitudes are greater than the spatial resolution goals. The brain is incompressible but viscous, thus one expects improvements in compensation methods will be needed for studies of brain stem nuclei where the major motions occur due to respiratory and cardiac influences on cerebral spinal fluid [41]. These motions can be measured by phase maps and navigator pulse methods, and during MRI studies they must be compensated if 100-μl resolutions are to be realized. However, successes have been realized in achievement of 0.2-mm isotropic spatial resolution in the human brain [42].

Human brain structure and function research enabled by ultrahigh magnetic fields

Sensitivity increases from ultrahigh magnetic fields

The opportunities for research in human brain structure, function, and chemistry created by magnetic fields much higher than exist today are tremendous, as many neurophysiology and neuropsychiatric questions cannot be approached by any other methods. Beyond 7 T there are seven MRIs: four large-bore at 9.4 T (one currently under repair after a quench), one at 10.5 T, and two being installed at 11.7 T. Recent measurements up to 9.4 T in the human head with multichannel array receivers suggest an SNR increase that scales as $B_0^{1.65}$ for protons [1] close to the predictions of Hoult and Richards [43] of a 7/4th power increase. Measurements of SNR gains above 9.4 T will depend on the imaging sequence and the influence of relaxation parameters. Simulations show more of a linear relationship with field increases beyond 9.4 T [44], and our (VS) measurements in the rodent brain show a slightly better than linear gain of SNR with field increases from 9.4 to 21.1 T [45]. In addition to SNR gains measured for tissue water detection sensitivity, there will be a significant increase in signal relative to background due to changes in relaxation parameters of metabolites and contrast agents relative to tissue water as well as the gains from innovative RF transmit and receive coils.

Brain structure and the BOLD effect

Since its original description in 1991, functional magnetic resonance imaging (fMRI) has revolutionized the study of normal and pathologic human brain function. While its precedent in PET imaging predated it by more than a decade, it was the non-invasive nature of the MRI experiment, and the concomitant acquisition of superimposed high-resolution brain anatomy, that led fMRI to become the principal tool for human cognitive neuroscience and the means by which we evaluate distributed brain function in patients clinically and in human subjects for brain neuroscience. Connecting this “systems level” study of brain function (visual, somatosensory, memory, etc.) to insights being gained in cellular and local neural circuits will require bridging two orders of magnitude in spatial scale.

Ten years ago the expected BOLD fMRI resolution was at the level of 2 mm at a time when gradient echobased acquisitions were used [46]. Since 2007, numerous columnar- and layer-specific structures with spatial features much smaller than a millimeter have been mapped by BOLD fMRI using strategies that selectively suppress the “draining” vessel contributions using several different techniques, such as using spin-echo protocols rather than gradient echo BOLD [47–51]. These techniques allow approaches to the theoretical physiological spatial resolution dictated by intercapillary distance (~25 μm). Resolutions less than 2 mm have been mapped by exploiting the fact that the draining veins that confound the BOLD fMRI spatial resolution are located on the pial surface and affect primarily the upper layers of the cortex; thus, they can be eliminated from the analysis in high-resolution data, by “stripping off” the upper layers and performing the fMRI analysis on the rest of the cortex [52]. We can anticipate that studies of small groups of neurons in anatomical structures (e.g., Fig. 4) will expand to studies encompassing thousands or more neurons in the next few years, at least in rodents and select human settings [47]. But connecting these local circuit functions to the widely distributed and highly interconnected activity of the human brain will require non-invasive imaging at spatial scales where coordinated neural activity across these large clusters of neurons occurs.

For reduced field-of-view and partially parallel acquisitions an isotropic resolution of 0.65 mm at 7 T has been reported [53]. Most studies reported recently use a voxel size from 0.75 to 1.5 mm [48–56]. This method is at best marginal for reaching the level of ensembles of neurons that perform similar and elementary computations, but is capable of interrogating local circuits. If we assume linear gains in SNR and BOLD contrast, 14 T translates into fMRI studies at a resolution with about 0.1 μL voxel volume. This resolution would allow sampling of the six cortical layers defined by the neuron types across the cortical thickness simultaneously with several voxels across a cortical column on the tangent to the cortical surface. We anticipate that at magnetic fields in excess of 14 T, in vivo measurements at a voxel resolution of ~0.05 μL will be feasible, and RF penetration is not expected to be a problem [38].

Neuronal architecture

Diffusion-weighted imaging (DWI) provides a unique view of white matter in the brain through measurement of restricted translational diffusion of water by the axons [57, 58]. This allows the mapping of long-range connectivity and provides a structural correlate to function connectivity derived from fMRI. But DWI in clinical scanners (up to 3 T) has a spatial resolution limit of ~2 mm, so fiber tracking with DWI resolves only large bundles of white matter axons. The complex fibrous structure of white matter can be further resolved using methods of high angular-resolution diffusion-weighted imaging (HARDI) to determine the water displacement probability function [59]. DWI for tractography with 1-mm isotropic resolution and full brain coverage is feasible [60] and 0.65-mm isotropic partial brain coverage has been reported [53]. But important small fibers, which require spatial resolution ≤0.5 mm, cannot be resolved. Higher resolution studies using brain stem tissues ex vivo at 11.1 T point to the requirement of isotropic resolution of 0.33 mm to resolve important small fibers [61]. Recently, ex-vivo HARDI measurements of the human hypothalamus (Fig. 5) were demonstrated at 17.6 T by one of the authors (TM) and

University of Florida colleagues [62]. A fresh surgically-resected anterior temporal lobe section containing the hippocampus of an epileptic patient was imaged for 5 h at 17.6 T with a maximum diffusion gradient of 394 mT/m and short echo time of 28 ms. Isotropic resolution was 0.22 mm. The resolution allowed a clear delineation of structure and white matter organization not evident in in vivo DWI.

In principle, resolution of <0.3 mm should be achievable at fields of 14 T and greater. The importance of achieving much better resolution than available in the past is demonstrated by the discovery of previously unknown neurite orientations in the human cortex using cadaver samples at 9.4 T and a gradient of 1500 mT/m [63].

As discussed under *Gradient Coils* there are no known barriers to construction of gradient coils that can operate at fields of 7 T and beyond. Preliminary successes in current experiments at 7 T and beyond, along with parallel acquisition with RF shimming and compressed sense strategies [4, 56] give promise for DWI tractography at fields of 14 T and greater.

New horizons for in vivo proton spectroscopy

At fields of 14–20 T identification of the spatial distribution and dynamics of small molecules not heretofore measureable can be realized for the first time in human brain neurochemistry. Numerous synergies contribute to this, including the enhanced sensitivity provided by ultrahigh magnetic fields, the larger spectral dispersion aiding significantly in the suppression of water resonance interferences, and the divergence between water relaxation properties and those of brain metabolites. Tailored pulse sequences can enhance metabolites of interest because the relaxation times and the sensitivity of high magnetic fields reinforce one another significantly. When the bulk of the water and macromolecular reservoirs remain essentially un-perturbed, the metabolites' T_1 relaxation times are shortened by crossrelaxation and/or chemical exchange effects, even in the case of non-labile methyl sites. Additional benefits at ultra-high fields are the major shortening of water's T_2 relaxation time relative to metabolites leading to negligible water signals at suitable echo time (TE) experiments. Also, at very high fields the longitudinal relaxation time of water is on average 2–4 times longer than the T_1 of metabolic peaks. The reasons underlying these effects are counter-intuitive, but the result is a synergy that delivers unexpectedly high MRS sensitivities and a complete avoidance of water-induced disturbances. We demonstrated these remarkable improvements to ^{1}H MRS at 21.1 T in live rodent brains (Fig. 6) with spectra acquired in 6 s from a 125-μL volume and with SNR of 50:1 [64]. With this unprecedented SNR we can determine single-metabolite diffusion, providing clues into neuronal microstructure that might be obscured due to the contribution of bulk water. With this capability, ultrahigh-field ^{1}H MRS/MRSI of the central nervous system (CNS) could become an enabling technology that could map with unprecedented spatial resolution, metabolites heretofore not detected by any other method in the living human brain, and could thus lead to new biomarkers of brain function that have previously escaped detection.

Chemical exchange saturation transfer

The improved sensitivity and spectral resolution of high-magnetic-field MRI/MRS enables quantification of brain metabolism of neurotransmitters such as glutamine, glutamate, and GABA, as well as neuronal markers such as NAA and glial cell metabolites such as myoinositol. Added to the sensitivity advantage of high magnetic fields is the NMR method of Chemical Exchange Saturation Transfer (CEST) that was proposed in 1998 to image water proton exchange between tissue water and metabolites such as amino acids, sugars, nucleotides, and heterocyclic ring chemicals [65–67]. CEST employs the transfer of magnetization from low concentration metabolic pools of exchangeable protons (amide, imino, and amine protons) to the bulk water proton pool. The combination of high field and CEST provides the opportunity to indirectly detect low concentration labile protons, such as protons of amine (NH_2), amides (NH), glucose (glucoCEST), glutamine (gluCEST), glycogen (glycoCEST), urea (urCEST), etc. These metabolites are normally difficult to observe at high spatial resolution by conventional MRI. As exchangeable protons have different resonant frequencies from that of free water, they can be selectively saturated using a compound-specific radio-frequency pulse. Due to the exchange between the two pools of protons, saturation can be transferred from one group to the other, leading to a decrease in the free water signal, that is the hallmark of the CEST effect. Given shifts δ_a and δ_b connected by an exchange rate $k_{ex} \leq |\delta_a - \delta_b|$, the range of processes that can be targeted in this manner is aided by the increased chemical shift separation (in Hz) between the two pools of protons. The lengthening of the T_1 relaxation time of water molecules with increasing magnetic fields leads to an increase in sensitivity of CEST, because the degree of magnification arising from this effect is proportional to $k_{ex} T_1$. The increases in SNR, spectral dispersion, and T_1 relaxation lead to a field dependence that is better than B_0^2. When coupled to higher-order shims, parallel transmission and reception, and other instrumental improvements, this should make it possible to establish in vivo high-resolution maps of certain molecules such as glucose, glycogen, or glutamate, which play a major role in energy metabolism pathways.

CEST does not require inordinately large increases in power over that required for non-CEST imaging and spectroscopy. The actual SAR increase (or deposition of energy) to execute CEST depends upon the proton exchange rate and T_1 times of the species under investigation. Slowly exchanging species require very little power while fast exchanging species require much more power. Many of the endogenous protonated species in exchange with water protons are quite slow, with rates on the order of a few msec. Those species can be activated with very weak RF pulses (e.g., 0.6–0.9 mT pulses were reported in a human study at 7 T [68]). This can be accomplished quite easily using a variety of low-B_1 approaches such as a train of 25 ms pulses of ~1 μT peak amplitude, which leads to a slow (e.g., 3–4 s) build up of a saturation steady state that is maintained for the frequency being studied. When added to the use of both parallel acquisition and compressed sensing, this will make CEST techniques easily assessable at much higher fields than those currently available.

In summary, the CEST effect shows a marked amplification with magnetic field strength for several reasons including better spectral resolution, a larger range of proton exchanging

species amenable for CEST contrast, the increase of water proton T_1, and the usual increase in sensitivity gained by higher B_0. Such multiple effects mean that the overall quality of CEST experiments will dramatically increase with B_0. We verified this using the NHMFL's 21.1 T system in collaboration with the University of Texas Southwestern group. CEST mapping of protein amide protons in the human brain has been successful at 7 T [67]. The new low-power pulsed CEST approach performed in six human subjects at 7 T showed a relayed-Nuclear Over-hauser Enhancement CEST effect, that was about twice as large as the CEST effects downfield and larger in white matter than in gray matter [68].

CEST measurements with other nuclei (^{31}P CEST) is also possible at ultrahigh fields, and given that the ^{31}P resonances of ATP, ADP, and AMP are resolved at ultrahigh fields, CEST could provide an efficient, non-invasive diagnostic tool for quantitative bioenergetic measurements in the human brain.

Brain phosphorus bioenergetics (^{31}P)

When performed at ultrahigh fields, the increase in SNR and in chemical shift resolution of ^{31}P nuclei in compounds of the brain should enable us to study dynamic brain functions ranging from the ability to show regional changes in all the phosphorus compounds to definitive studies of small molecule patterns associated with brain function. Adenosine triphosphate (ATP) production is vital to cellular functions, especially in neurons, which have a continual need for energy resources to restore basal transmembrane ionic electrochemical potentials. Neurons use ATP largely produced through oxidative phosphorylation. ATP is transported out of the mitochondrial matrix into the cytosol and used by a variety of enzymes, most prominent of which is the Na^+/K^+ ATPase. We have collected ^{31}P spectra at 9.4 and 16.4 T from cat brains that prove we can measure relative concentrations of all the important phosphorylated species at ultrahigh fields. Human brain studies at 9.4 T have shown the ability to map the distribution of the major components of ATP kinetics [69]. The frequency of ^{31}P at 11–21 T (190–360 MHz) is on par with ^{1}H frequencies at 4.5–8.5 T.

Relaxation rates of most ^{31}P nuclei in brain metabolites become longer at higher fields [70]; thus, we expect to be able to map ATP synthesis rates regionally in the human brain. It may also be possible to resolve mitochondrial versus cytosolic ATP and Pi resonances in the human brain at ultrahigh fields. We expect that high-field chemical exchange saturation transfer (^{31}P CEST) could resolve all ATP, ADP, and AMP signals, and thus become an efficient, non-invasive diagnostic tool in quantitative bioenergetic measurements. Acidic (low pH) environments, an aftereffect of cell metabolism, can also be quantified using ^{31}P MRS. At the intermediate frequencies of these nuclei, we do not expect major challenges with respect to RF penetration and homogeneity, as many of these problems are well understood and have been solved from experiences with 1H at 7 T (300 MHz).

Brain Na^+, K^+-ATPase activity mapping

An alternative to mapping brain ATP enzymatic fluxes with lower-resolution saturation transfer ^{31}P MRSI, is the use of Dynamic-Contrast-Enhanced (DCE) methods for mapping trans-capillary wall water turnover. DCE-MRI is a minimally invasive MR method

consisting of acquiring T_1-weighted MR images before, during, and after IV injection of a gadolinium-based contrast agent (CA). The quantification results from pharmacokinetic modelling as the CA distributes through the blood plasma in the normal brain. From the kinetics, the mean intra-capillary water molecule lifetime can be inferred, with a spatial resolution ≤1 mm. Its reciprocal is proportional to Na^+, K^+-ATPase (NKA) turnover, a process involving active trans-membrane water cycling [71]. NKA is the brain's most vital enzyme, consuming over 50 % of ATP per unit time. The DCE-MRI method involves analysis of ^1H_2O signals obtained during CA transit through brain capillaries. Neuronal and neuroglial cells have an exquisite metabolic synergy with capillary endothelial cells, and this couples the mean rate constant for equilibrium capillary water molecule efflux, k_{po}, to its cell membrane analog, k_{io}. It is the latter that is proportional to NKA turnover [72]. The first normal human resting-state brain k_{po} map (Fig. 7) has been obtained at 7 T [71]. It is interesting that NKA activity per capillary is greater in white matter (WM) than in gray matter in the awake patient. The hot spots may reflect WM tracts connecting cortical "rich club nodes," which participate in many different transient resting-state functional circuits. A study planned by the Oregon authors, Rooney and Springer with the University of Minnesota to define the capabilities of this new high-resolution metabolic neuroimaging method at 10.5 T awaits IRB approval. At ultrahigh magnetic fields, brain k_{po} maps with sub-mm spatial resolution can be obtained and compared to ^{23}Na maps, whose spatial resolution will be lower. These comparisons can validate the hypothesis that elevated tissue sodium concentration (TSC) represents a reduced trans-cytolemmal sodium gradient (altered NKA turnover) more than extracellular swelling [72]. These alternatives cannot be discriminated by simple TSC alone. Higher field will lead to improved NKA turnover quantification because tissue generic macromolecule relaxivity decreases with the increased field faster than does contrast agent relaxivity [73, 74]. Thus, the fractional contrast change increases with B_0. These observations argue for human brain studies at fields higher than 7 T.

Functional brain map of glucose oxidation

Using uniformly labeled ^{13}C glucose infused into human subjects, we have measured fluxes on pathways from glucose to pyruvate, pentose phosphate, the TCA cycle, bicarbonate, and glutamate at 7 T with 5 min acquisitions (Fig. 8). These whole brain studies can become regional functional mappings at the proposed increase in magnetic fields with almost tenfold sensitivity increases. Pyruvate is at the branch point in the bioenergetic paths for biosynthesis of amino acids, fatty acids, and carbohydrates. A method for mapping the regional fluxes of pyruvate to specific biochemical products will provide a powerful means of understanding bioenergetic responses triggered by physiochemical changes. Of importance to human behavior is that relative fluxes are known to be affected by brain stimulants such as cocaine [75] and amphetamines [76]. A second powerful use of ^{13}C MRS/MRI at ultrahigh fields is the potential to image glucose oxidation regionally in the human brain. Figure 8 shows an unlocalized ^{13}C spectrum of the human brain after a subject was infused with [U-^{13}C] glucose for 2 h. This spectrum was acquired in 5 min at 7 T without proton decoupling. The glutamate C5 resonance reflects glycolytic conversion of [U-^{13}C]glucose to [U-^{13}C] pyruvate followed by the oxidation of pyruvate in the TCA cycle, while the strong bicarbonate resonance reflects total oxidation of glucose through the

pentose phosphate pathway plus the TCA cycle. If other substrates compete with glucose for energy, this would be reflected in the ratio of glutamate C5 to bicarbonate ratio as measured by MRS. In principle, since this experiment does not require proton decoupling, one should be able to image bicarbonate and use this as a biomarker of regional glucose oxidation in human brain.

MRI of X-nuclei at high magnetic fields

The justification for metabolic imaging of non-proton elements such as sodium, potassium, and oxygen, in addition to carbon and phosphorus of metabolically active compounds, comes from their central roles in tissue metabolism. The potential energy stored in the sodium, potassium, and other ion gradients across cell membranes are essential components of brain physiology. Another naturally occurring and NMR-detectable element is oxygen-17, whose endogenous or injected signal opens the opportunity for in vivo studies of oxidative metabolism of the human brain. The drawback for NMR in vivo studies of elements in addition to protons is the low abundance and overall low sensitivity (see Table 1) that limit the spatial resolution for MRI and MRS that require prohibitive times for human subject observations. It is important to note that the major difference between proton MRI and MRI of nuclei such as Na, K, Cl, and O is that image contrast for ^{1}H-MRI is determined by the nuclear relaxation properties of the regional tissue water, diffusion anisotropy, and susceptibility of the tissue components, whereas X-nuclei MRI gives information regarding the concentration of the element and its spectral position as well as the relaxation dependent information about the environment.

The most straightforward strategy for overcoming this sensitivity challenge is to increase the field strength, as has been demonstrated by the increases in field strength over the last 35 years for proton MRI in moving from less than 0.35 T to 9.4 T for human studies, and soon to 10.5 and perhaps 11.7. For considerations presented in the first section of this paper, the technology that would allow progression beyond 11.7 T is now available, giving encouragement to brain neurochemistry studies at fields of 14 T and above. A realistic goal is to achieve a spatial resolution of $2 \times 2 \times 2$ mm^3 and a data acquisition requirement of less than 30 min. This goal can almost be reached for ^{23}Na MRI at 9.4 T but not for ^{17}O or ^{39}K MRI. The SNR for ^{17}O is three times lower than ^{23}Na, and for ^{39}K is 24 times lower (Table 1). In addition, many of the attractive new elements in Table 1 have quadrupole moments that necessitate special pulse sequences. But even here, progress has been made to achieve in vivo studies as shown below. However, the opportunities for fundamental studies of brain physiology require higher magnetic fields beyond current ultrahigh fields for human imaging.

^{23}Na MRI at ultrahigh fields

Tissue sodium concentration (TSC) and its derived parameter of cell volume fraction (CVF), as measured by quantitative ^{23}Na MR imaging, provide unique information not only regarding sodium ion homeostasis but also the status of CVF and its dependency on disease and aging [77, 78]. In the normal human brain, the global TSC value is 35 ± 3 mM and is independent of age. This reflects a cell density or CVF of about 81 ± 2 %. It is of great interest that TSC and CVF do not change during normal aging [78] (Fig. 9). Despite the loss

of brain volume that occurs with normal aging, the cell density remains the same as the neurons become smaller with less dendritic arborization and fewer synapses. The extracellular matrix (ECM) that forms the interstitial support structure of the brain must also be reduced in volume, presumably by normal turnover processes that are regulated by neuronal cell volume. This finding from ^{23}Na MRI is the in vivo confirmation of results reported from neuropathology using design-based stereology and cell counting techniques. This adaptive process of aging suggests the hypothesis that CVF stability has a fundamental role in maintaining the energy efficiency of ion homeostasis that supports brain function. This hypothesis can be tested using the cerebral metabolic rate of oxygen consumption ($CMRO_2$) measured by ^{17}O MRI, as discussed below. But higher fields than 9.4 T are needed to obtain the quantitative data for input to physiological models of normal and abnormal human brain functioning.

Feasibility of imaging ion gradients

Another major opportunity is the ability to quantify electrochemical gradients within different tissue compartments of the human brain. The significance of 20 T is that the improved SNR of this higher field can provide opportunities for spin manipulation of the ions (^{23}Na, ^{39}K, and ^{35}Cl) that maintain the electrochemical potentials in the brain. These ions have spin 3/2 and thus are sensitive to microscopic, local in vivo electric field gradients. This quadrupolar moment interaction leads to spectral shifts and spin interactions that can be detected, using tailored RF pulse sequences to measure intracellular and extracellular concentrations without using exogeneous chemical shift agents. Quantification of the ion concentrations has the potential to map ion gradients between different compartments of the brain. Sodium imaging [77–81], potassium imaging [82, 83], and chloride imaging [84] have been accomplished in the human brain at 7 T and 9.4 T. However, to exploit multiple quantum imaging methods to determine the separate concentrations of these ions in the intra- and extracellular compartments, the sensitivity must increase substantially. A field increase from 7 to 20 T can realize an increase in SNR of 6 that reflects a 36-fold decrease in acquisition time based on the theoretical prediction of the 7/4 power-dependence of field strength [43]. Preliminary multiple quantum experiments at 21.1 T (Fig. 10) have demonstrated detection of sodium and potassium ions in the rodent head. These represent different in vivo electric field gradient environments and are related to intracellular and extracellular compartments. Previous experiments in the beating rodent heart validated the triple quantum MR signals against chemical assays [85]. This will also be required in the brain. The new methodology used to acquire data in Fig. 10 is significantly more efficient in acquiring TQ signals than earlier suggested methods based on MR signal filtration. This approach will be extended to spatial imaging via the back-projection method of simultaneously detected SQ and TQ signals to investigate the resolution limits and time vs. SNR at fields of 17.6–21 T.

The determination of ion concentration gradients across cell membranes is of fundamental importance, as gradient mapping gives non-invasive data similar to invasive electrophysiology studies of the human brain. Although much work is still required, the

principles for achieving this goal with MRI are understood. The SNR of ultrahigh field >14 T is needed [86].

^{17}O MRSI and MRI at ultrahigh fields

Oxygen-17 MR imaging can detect small dynamic changes of metabolism via the appearance of $H_2^{17}O$ resonances, as has been done at 9.4 T in the human brain following inhalation of $^{17}O_2$ enriched gas [87]. Increases in SNR from higher fields will allow spatial imaging approaches to measure the regional cerebral metabolic rate of oxygen consumption. The relaxation times (T_1, T_2 and T_2*) of O_2 are relatively short, but these relaxation times are field independent [87]. Imaging regional cerebral oxygen utilization rates during human brain function would provide for the first time quantitative regional measures of cognitive performance across the neural network being stimulated. Such measurements should be feasible at fields ≥14 T based on previous experiments at 9.4 T [88]. Oxygen utilization can be a functional imaging parameter that is directly linked to the metabolic processes that subserve neuronal activity. The quantitative accuracy, spatial resolution, noninvasiveness, and specificity make this functional imaging method far superior to positron tomography with $^{15}O_2$. Linking MRI determined perfusion, oxygen utilization, phosphorylation potential [ATP]/[ADP] × [PI], and carbohydrate/FFA flux can provide a more complete picture of brain metabolism under different states of brain activity than has existed in the past.

Mapping the electrical properties of the brain

At the operating frequencies associated with high- and ultrahigh-field MR, interactions of magnetic and electric fields with dielectric tissues result in substantial distortions of those fields and of corresponding RF coil transmit and receive sensitivities. These distortions are the origin of “RF shading” artifacts typically encountered at high field strength, but they also contain potentially valuable information about tissue. Indeed, it has been shown that careful measurements of the curvature of RF fields in MR experiments may be used to map the quantitative values of tissue electrical properties, including both conductivity and permittivity [89–93]. Since the RF field distortions increase with increasing frequency, electrical property mapping techniques based in quantifying these distortions should in principle improve with increases in main magnetic field strength. One caveat is that some of the symmetry assumptions underlying most current electrical property mapping techniques tend to break down at high frequency [89–92]. However, generalized techniques have been proposed which eliminate such symmetry assumptions [93] and which may be expected to achieve improved robustness and spatial resolution at ultrahigh field strengths. Electrical property mapping holds promise as a new window into brain tissue physiology, and it has the potential to be used for functional brain imaging in 14–20 T studies.

Physiological effects and safety at 14 T and above

Background

The study of physiological effects on human subjects from static magnetic fields, switched gradient magnetic fields, and radiofrequency fields (15–850 MHz) used in MR commenced 35 years ago [94, 95]. A synopsis of the scope of the relevant biophysics was reported by us in the 2013 National Research Council (NRC) report on high magnetic field science [96]. Of

the reported and measured effects in human subjects (e.g., vertigo, nystagmus, absorbed RF power, peripheral nerve stimulation, and torque on sensory elements with susceptibility anisotropy), none has been limiting or considered harmful at allowed limits to 9.4 T. U.S. FDA investigational device exemption (IDE) has been approved to 9.4 T, and evaluation of the new threshold of 10.5 T began in 2015 at the University of Minnesota.

Fortunately, we already have in-vivo MRI/S data on rodents at 21 T with no evidence of health effects except a temporary effect on the vestibular apparatus. No long-term negative health effects on human subjects have been validated up to 9.4 T [96–100]. Safety and potential health effects concerns associated with field strengths to 14 T and above include the potential for genotoxic effects, RF heating at frequencies up to 850 MHz, and nerve stimulation from switched magnetic field gradients required to image neuronal architecture at high resolution.

Known physiological effects include induction of peripheral nerve stimulation at high rates of field change [101], effects on vestibular function [102], and rodent behavioral avoidance [103, 104]. In the sections below, these and other biophysical phenomena will be presented relative to possible effects at fields of 14 T and above. Reports of other effects, such as temporary cognitive changes in humans exposed to magnet fringe fields and inconsistent reports of sensing high magnetic fields or field gradients, have been made by some subjects inside and in the fringe fields of 7 T clinical magnets. These could be related to some of the biophysical phenomena outlined below.

Peripheral nerve stimulation is dependent on the rate of field change (e.g. 60 T/s for the human thorax) and the diameter of conductive path loops [101]. This effect does not depend directly on the static field magnitude, but the volume forces (diamagnetic forces) do depend on both the gradient and the static field leading to a time and space varying force that can account for a number of physiological phenomena depending on the susceptibility anisotropy of sensory elements in the head. These effects are not currently known to be dangerous, but the forces scale with field, and thus further experiments are needed. Gradient coil designs can take advantage of the fact that the E-fields induced are proportional to the current loop diameters that are smaller than those associated with the body and with contemporary body gradient systems.

Static field effects

A first concern of very high magnetic fields is the danger from ferromagnetic materials including tools, metal furniture, and other ferromagnetic objects that can become projectiles [102]. A life-threatening danger to personnel is metallic implants including pacemakers and wound clips. Other than the fact that the forces will be greater when the field and the field gradient become larger, one does not expect increased hazards from forces at 20 T. The current screening of individuals before entering the magnet is an adequate safeguard against harm arising from pacemakers and other implanted ferromagnetic objects. There is a potential problem associated with magnetic particles found in nature such as the magnetosomes seen in bacteria (Fig. 11). Magnetite particles exist in the human brain (meninges) [105], the estimate is 50 ppm. To what extent a high field and field gradient product can induce these particles to overcome the restraint of local adhesive and tissue

viscous properties on prolonged exposures to 20 T can be readily determined by experiments at existing high-field magnets at the NHMF in Tallahassee, Fl.

Effects on molecular assemblages with susceptibility anisotropy—The magnetic energy associated with the orientation changes of molecular assemblages is proportional to the magnetic field squared, as does the rate of orientation change in accordance with the following relationship.

$$\mathrm{d}\Phi/\mathrm{d}t = -B^2\left[V(\chi_\mathrm{a}-\chi_\mathrm{r})\right]\ \sin 2\Phi/2\xi \quad (1)$$

where $\mathrm{d}\Phi/\mathrm{d}t$ is the angular change with time, B is the magnetic field, V is the volume of the assemblage, χ_a and χ_r are axial and radial susceptibilities, respectively; and ζ is the rotatory frictional coefficient that is proportional to viscosity [107]. Retinal rods in a petri dish are oriented by 90° in less than 10 s in a field of 1 T. Not included in this expression are the overwhelming restraining adhesive forces associated with organized tissues and an expected frictional drag dependence on the square of angular velocity.

Volume forces on diamagnetic tissues—Volume force is the product of tissue susceptibility, the B field, and the B *field* gradient.

$$F = \chi/\mu_0 B_0 \times \mathrm{d}B/\mathrm{d}z,$$

Here, χ is susceptibility (dimensionless), μ_0 is magnetic permeability ($4\pi \times 10^{-7}$ NA^{-2}), B is the main field, and dB/dz the spatial gradient. For tissue the formula is:

$$= \left(-9\times10^{-6}/4\pi\times10^{-7}\right)B^2/\mathrm{m} = -7.2\times T^2/m \text{ or } \left(\mathrm{N/m^3}\right) \quad (2)$$

Curves calculated from equation [2] are shown in Fig. 12. From our calculations using magnetic field data from Houpt et al. [104], the rodent avoidance volume force is 70 T^2/m. The cause for the avoidance could be an effect on the vestibular apparatus (vide infra). The volume force threshold for human tolerance could be the key determinant of magnet design, as the gradient can be controlled by the bore length.

Differences in forces on adjacent tissues are dependent on the small differences in susceptibility including layers of the human cortex. Shear forces between tissue and fat or tissue and bone might be sensed but not be uncomfortable. But the susceptibility differences between iron-loaded tissues and adjacent tissues such as the cerebral cortex [108] and other tissues [109] will need evaluation. The importance of these differences will need to be ascertained before human subject exposures to ultrahigh fields and high-field gradients.

Note at the top of Fig. 12, the repelling volume force on a frog in a 16.4 T magnet is equal to density × Earth's gravitational acceleration, and at a certain position the frog will levitate [110].

Lorentz forces on ionic currents in nerves

Lateral forces on nerve axons at 20 T—The propagating current densities for neurons are of the order 8–10 A/m^2, and the E-fields downstream are about 8 V/m. Recall the peripheral nerve stimulation threshold from dB/dt is 6 V/m [101]. Using the derivation of Roth and Basser [111] we calculate the lateral displacement as 64 μm. The operational equation is:

$$d=(F/4P)a^2 \ln (b/a) \quad (3)$$

Here, d is the displacement, F is the volume force based on a current density of 10 A/m^2 and a B field of 20 T, P is the shear modulus (10 kP), a is the nerve radius (2 mm), and b is 25a. The displacement at 20 T is 64 μm. This displacement and other calculations by Roth and Basser [111] are less than would be detected in MRI images and are not of health significance.

Nerve impulse conduction speed effects—The Lorentz effect or force on moving ions in a magnetic field can result in a slowing of nerve conduction velocity. The motion of sodium and potassium ions during nerve conduction can be pictured as small current loops along the axis of the conducting nerve fiber. If a field is applied at right angles to the nerve fiber, one can expect the ion current paths will be distorted. An ion of charge e in an electric field, E, and magnetic field, B, will have forces F_e = eE and F_m = e(Vd)B, respectively. Here, V_d is the drift velocity of the ions. Wikswo and Barach [112] show V_d is between 0.033 m/s and 6.6 × 10^{-5} m/s depending on the values chosen for the estimation. These considerations suggest that a 10 % change in nerve conduction velocity will occur at 24 T.

Induced electric potentials—Faraday law

Blood is an ionic conductor, and its flux in a magnetic field will result in an induced voltage, which is proportional to the flow (current) and the diameter of the vessel (e.g., the aorta) if the flow is orthogonal to the magnetic field:

$$V=\mathrm{vBd}. \quad (4)$$

For the human aorta, a flow v = 1 m/s in a field of 20 T and diameter of 0.016 m gives the emf as 0.32 V. No problems with cardiac rhythm have been noted in human exposures of many subjects to 9.4 T [100]. Tenforde [113] predicted on theoretical grounds a current density near the sinoatrial node of the heart of 220 mAm-^{2} on the assumption that significant leakage currents occur, but the aorta specific resistance is six orders of magnitude larger than blood, thus the predicted current densities cannot occur. The induced voltage scales as vessel diameter. The evaluation of untoward electrical phenomena does require detailed modeling with high spatial resolution of the specific resistivity. A multitude of canine studies have been completed at 11.1 T with no cardiac events observed (University of Florida, Gainesville).

Induced E-fields from time varying gradients—An E-field of 6 V/m induced by 60 T/s near a 30-cm diameter conducting body will cause a sensation of an electric shock [101]. The governing physics are represented by the Maxwell–Faraday equation that equates the electric field to the diameter of a loop of body conductor exposed to the stimulating coil.

$$V/m = -\,\mathrm{d}B/\mathrm{d}t \times r/2, \quad (5)$$

where *dB/dt* is the rate of the magnetic field change and *r* is the object radius seen by the inductor. Note that a change in the area of a conductor in constant *B field* will also induce an E-field; thus, chest expansion and cardiac chamber size changes will result in a potential superposed on the standard electrocardiogram recording in addition to the E-field induced by moving electrolytes (i.e., the blood flow).

Visual sensations known as magnetophosphenes that can be induced at about 2 T/s involve a different physical mechanism than the peripheral nerve stimulation at 6 T/s. This phenomenon has been studied since visual phosphenes were noted in 1896 by d'Arsonval, who moved a magnetic field source near the eyes [114]. The mechanism is not as simple as suggested by equation [5] because the threshold for visual sensations is dependent on reaching a field of at least 10 mT with a rise time of approximately 2 ms and a repetition rate of less than 30 per second [115]. These dependencies can be understood if the mechanism is a mechanical distortion of retinal components from susceptibility anisotropy. Direct electric voltage application to the head can induce phosphenes but the current densities of 17 $\mu A/cm^2$ are much greater than the 2 $\mu A/cm^2$ that is inferred from magnetic field changes. The emphasis on the mechanisms for phosphene observations is relevant to understanding other sensory phenomena that might manifest at 20 T where larger fringe fields and B fields are expected than have been experienced in the last 35 years of investigations.

Magnetohydrodynamic effects—A conductor flowing in a magnetic field will experience forces that will resist flow, thus to maintain adequate tissue perfusion the body will increase blood pressure. To model this effect, the Lorentz force and Ampere's law are incorporated into the Navier–Stokes equation of motion that relates the pressure gradient to velocity, viscosity, permeability, and volume force. A second equation of motion uses Faraday's, Ohm's, and Ampere's laws to relate the magnetic field with conductivity. While there is a rich literature giving approximate solutions showing significant pressure effects at fields up to 15 T, the exact solution shows the pressure change is only 0.2 % at 10 T. The only experimental data that fits this exact solution are our observations at 4.7 T using a saline solution flowing at a volume flow of 7 L/min in a 0.016-m tube orthogonal to a 4.7 T field [116].

Vestibular organ effects—The inner ear organ responsible for sensing position as well as sound has hair cells bathed in fluid. The differential motion between fluid and 1 micron sensors sends signals to the brain. These signals coordinate with visual and peripheral nerve sensors. Either susceptibility anisotropy or Lorentz forces may be responsible for sensations of dizziness and nausea experienced at high fields. A wide variety of experimental observations implicate the vestibular apparatus for the variety of symptoms and signs

manifested by animals and human subjects in high magnetic fields, as well as in the fringe fields of high-field magnets where forces can cause small but physiologically significant relative tissue motion. Observed symptoms and signs include avoidance by animals of high fields and field gradients [104], animal head tilt while in a homogeneous field, and turning behavior of animals after exiting high magnetic fields [103] as well as other temporary effects [117].

Human subjects have definite symptoms of nausea, vertigo, nystagmatism, and some reversible decline in cognitive function at fields of 4, 7, 8, and 9.4 T, e.g., [118–121]. Effects on the vestibular system are believed to underlie these phenomena. Definitive experiments that implicate the vestibular system in animal behavior showed no effects if the vestibular system is ablated [122].

The understanding of strong magnetic field effects on the inner ear has recently been significantly advanced by the observation of field-induced nystagmus in subjects in a strong magnet in a darkened room [123]. This is attributed to Lorentz forces on the steady currents produced by the continual depolarization of the hair cells. From the modeling and experimental work of Roberts et al. (wherein the force per cupula area was between 0.02 and 0.002 Pascal) it is concluded that the nystagmus can be accounted for by the Lorentz force because the force is 20 times the threshold for cupula stimulation. Pressures of 2 mPa are sufficient to stimulate nystagmus [124]. Additional human subject observations and analyses have further elucidated the physiology of nystagmus and the functioning of the vestibular apparatus [125].

RF power deposition

For low gamma nuclei (^{23}Na, ^{17}O, ^{35}Cl, and ^{39}K), the higher frequencies associated with 14 T and above should not present any new challenges, as patients have already been studied at these frequencies via ^{1}H MRI and MRS at lower magnetic fields. Special RF sequences such as those in the multiple quantum studies can go beyond current power deposition limits; thus, a particular focus in developing pulse sequences and RF coils will be to keep the SAR within allowable limits. Going beyond low gamma spins to proton imaging and spectroscopy at fields of 14 T and higher will require engineering of transmit and receive coil arrays, as well as methods of steering the RF fields and a general investigation of RF pulse sequence optimization [32, 38].

Magnetic field effects on molecules, molecular assemblages, and cells

In the sections above, the physics and physiology of static magnetic fields, switched gradient fields and RF interactions with biological tissues were outlined. The purpose of this section is to access the genotoxic and carcinogenic potentials for ultrahigh-magnetic-field MRI. For the past 35 years [94, 126], molecular, subcellular, cellular, and tissue effects of static and oscillating magnetic fields associated with MRI have been investigated. Effects of static magnetic fields ranging from 50 μT to 15 T on chemical and biologic systems were reviewed in 2008 by Okano [127]. There are as many positive as there are negative results in that review as well as in evaluations by others [128–130]. The current conclusion is that there are no health hazards from exposures up to 9.4 T. Non-controversial effects at the

macromolecular level are magnetic orientation or torque phenomena observed for large molecular assemblages in vitro such as chloroblasts and retinal rods based on magnetic anisotropy, as presented above [107, 109]. Orientation effects include structural changes in tubulin [131] and alterations of the cleavage plane in developing frog eggs [132], and could account for abnormalities in fibroblast and neuronal growth at fields up to 15 T reported in 2005 [133]. Other mechanisms include chemical separations, effects on hydrated states of ions [134], and significant prolongation of the lifetimes of oxygen- and nitrogenfree radicals arising from naturally occurring chemical transformations [127]. But these mechanisms have yet to be verified. No deleterious observations have been reported from extensive studies on rodents at 21.1 T by NHMFL investigators other than temporary effects on the vestibular apparatus. Reported gene expression effect in a transgenic plant Arabidopsis at 20 T [135] requires repetition with the incorporation of appropriate controls.

In the past few years, possible effects on DNA have been reported in blood samples (leukocytes) from subjects undergoing cardiac MRI protocols with and without injected contrast material. A summary of eight studies on human cells by Vijayalaxmi and co-workers [130] describes six studies that showed an increase in DNA double-strand breaks (DSB) or micronuclei (evidence of DNA damage) and two studies that showed no change. Three reports since that review showed no increases in DSB of subjects' blood following clinical MRI exposures [136–138]. Known causes of DNA DSB include UV, ionizing radiation (X-ray CT), virus infections, and environmental temperature [139] as well as beta blockers used by cardiovascular patients [140] and MRI contrast agents. Reports of DSB findings are in a background of 50 DSB per cell cycle, almost all of which are repaired [141], leaving experimentally visualized foci of breaks at the level of about 0.11 DSB per cell. A comparison of the quality of eleven experiments, absence of positive controls and lack of a mechanism to explain the positive results in six of 11 experiments leads us to the conclusion that there is no convincing evidence for a genotoxic effect from clinical MRI up to 7 T using DSB as an indicator.

Although animal studies to 21.1 T have not shown more than temporary physiological effects and there are no reports of harmful effects in human studies up to 9.4 T, published effects of fields of 10 T and beyond on replicating cells or growing tissues will require investigations to discover mechanisms that are not associated with the unnatural biological environment of the magnet and sample preparations ((e.g., free radical lifetime changes, electrolyte hydration, molecular assemblage structure alterations).

Organ studies beyond the brain

Organs of adult human subjects below the head and neck are targets for increased magnetic field investigations, but the technological and financial barriers are much larger than those for a head-only MRI system because the required magnet bore must be increased from 68 cm to about 98 cm. The current design for a head-only magnet at 14 T allows for shoulders and body entry into the bore, but the RF, shim, and gradient coils occupy too much space to allow body imaging. For example, the 11.7 MRI system at Iseult has a 90-cm bore [9]. The estimate of 98 cm for a body magnet at 14 T is based on the need for structural support of gradient coils due to the interactions with the high magnetic field as well as the requirement

for homogeneity. The Iseult body MRI homogeneous region is 10 cm in diameter [9]. If major improvements in HTS superconductor performance as well as reductions in manufacturing costs occur, then the following estimate might be too pessimistic. Scaling with the third power for the increase in bore from 68 to 98 cm results in a magnet mass and cost increase by a factor of 3.0. Nevertheless, the bore size of 68 cm is adequate for large animal studies that promise to uncover vital medical science regarding tumor metabolism, tumor heterogeneity, heart failure, renal metabolism, liver metabolism, skeletal muscle diseases, and spinal cord normal and abnormal functioning, for example.

The current hypothesis that magnetic fields beyond 10 T can prolong lifetimes of oxygen and nitrogen reactive species leads to the possibility of focused hyperthermia [142] for cancer treatment enhancement through treatment in a high magnetic field. This is another of many biological and medical science advancements that can be explored at fields of 14 to 20 T.

Summary

The focus of this review is on the rationale and feasibility of designing, building, and using magnetic resonance instruments to study in vivo the structure, neuronal circuits, and neuronal biochemistry of the human brain at magnetic fields of 14–20 T. Over the last 3 years there have been major developments in superconductor materials that enable the construction of magnets at much higher fields than exist currently. These advances also enable major instrumentation advances for NMR spectrometers and give confidence that the technology barriers and costs for human brain studies are no longer prohibitive. This review brings up to date the magnet technologies and the breadth of human brain scientific opportunities that no other method can provide. The assessment of physiological phenomena that human subjects will experience must go beyond current human studies at 9.4 T.

References

1. Pohmann R, Speck O, Scheffler K. Signal-to-noise ratio and MR tissue parameters in human brain imaging at 3, 7, and 9.4 tesla using current receive coil arrays. Magn Reson Med. 2016; 75(2):801–809. [PubMed: 25820458]
2. Uludag K, Muller-Bierl B, Uğurbil K. An integrative model for neuronal activity-induced signal changes for gradient and spin echo functional imaging. Neuroimage. 2009; 48:150–165. [PubMed: 19481163]
3. Ugurbil K, Xu J, Auerbach EJ, Moeller S, Vu AT, Duarte-Carvajalino JM, Lenglet C, Wu X, Schmitter S, Van de Moortele PF, Strupp J, Sapiro G, De Martino F, Wang D, Harel N, Garwood M, Chen L, Feinberg DA, Smith SM, Miller KL, Sotiropoulos SN, Jbabdi S, Andersson JL, Behrens TE, Glasser MF, Van Essen DC, Yacoub E, WU-Minn HCP Consortium. Pushing spatial and temporal resolution for functional and diffusion MRI in the Human Connectome Project. Neuroimage. 2013; 80:80–104. [PubMed: 23702417]
4. Setsompop K, Alagappan V, Gagoski B, Witzel T, Polimeni J, Potthast A, Hebrank F, Fontius U, SchmittF WL, Adalsteinsson A. Slice-selective RF pulses for in vivo B1+ inhomogeneity mitigation at 7 tesla using parallel RF excitation with a 16-element coil. Magn Reson Med. 2008; 60(6):1422–1432. [PubMed: 19025908]
5. McNab JA, Edlow BL, Witzel T, Huang SY, Bhat H, Heberlein K, Feiweier T, Liu K, Keil B, Cohen-Adad J, Tisdall MD, Folk-erth RD, Kinney HC, Wald LL. The human connectome project and beyond: initial applications of 300 mT/m gradients. Neuroimage. 2013; 80:234–245. [PubMed: 23711537]

6. Smeibidl P, Bird MD, Ehmler H, Dixon IR, Heinrich J, Hoffmann M, Kempfer S, Bole S, Toth J, Prokhnenko O, Lake B. First hybrid manget for neutron-scattering at Helmholtz Zentrum Berlin. IEEE Trans Appl Supercond. 2016; 25(3):1–6.
7. Martovetsky N, Michael P, Minervini J, Radovinsky A, Takayasu M, Thome R, Ando T, Isono T, Kato T, Nakajima N, Nishijima G, Nunoya Y, Sugimoto M, Takahashi Y, Tsuji H, Bessette D, Okuno K, Ricci M. ITER CS model coil and CS insert test results. IEEE Trans Appl Supercond. 2011; 11(1):2030–2033.
8. Lvovsky Y, Stautner EW, Zhang Z. Novel technologies and configuration of superconducting magnets for MRI. Super-cond Sci Technol. 2013; 26:171.
9. Vedrine P, Aubert G, Beaudet F, Belorgey J, Berriaud C, Bredy P, Donati A, Dubois O, Gilgrass G, Juster FP, Meuris C, Molinie F, Nunio F, Payn A, Schild T, Scola L, Sinanna A. Iseult/ INUMAC whole body 11.7 T MRI magnet status. IEEE Trans Appl Supercond. 2010; 20(3):696–701.
10. Bird MD, Dixon IR, Toth J. Large, high-field magnet projects at the NHMFL. IEEE Trans Appl Supercond. 2014; 25(3):4300606.
11. Miller JR, Bird MD, Bonito-Oliva A, Eyssa Y, Kenney WJ, Painter T, Schneider-Muntau H-J, Summers LT, Van Sciver SW, Welton S, Wood RJ, Williams JEC, Bobrov E, Iwasa Y, Leupold M, Stejskal V, Weggel R. An overview of the 45 T Hybrid magnet system for the new national high magnetic field laboratory. IEEE Trans Magn. 1994; 30(4):1563–1571.
12. Markiewicz WD, Dixon IR, Swenson CA, Marshall WS, Painter TA, Bole ST, Cosmus T, Parizh M, King M, Ciancetta G. 900 MHz wide bore NMR spectrometer magnet at NHMFL. IEEE Trans Appl Supercond. 2000; 10(1):728–731.
13. Wilson, MN. Superconducting magnets. Oxford University Press; Oxford: 1983. p. 46
14. Majkic G, Galstyan E, Selvamanickam V. High performance 2G–HTS wire using a novel MOCVD system. Appl Supercond IEEE Trans Supercond. 2010; 25(3):1–4.
15. Larbalestier DC, Jiang J, Trociewitz UP, Kametani F, Scheuerlein C, Dalban-Canassy M, Matras M, Chen P, Craig NC, Lee PJ, Hellstrom EE. Isotropic round-wire multifilament cuprate superconductor for generation of magnetic fields above 30 T. Nat Mater. 2014; 13(4):375–381. [PubMed: 24608141]
16. Nakashima T, Yamazaki K, Kobayashi S, Kagiyama T, Kikuchi M, Takeda S, Osabe G, Fujikami J, Osamura J. Drastic improvement in mechanical properties of DI-BSCCO wire with novel lamination material. Appl Supercond IEEE Trans Super-cond. 2015; 25(3):1–5.
17. Weijers HW, Markiewicz WD, Voran AJ, Gundlach SR, Sheppard WR, Jarvis B, Johnson ZL, Noyes PD, Lu J, Kandel H, Ba H, Gavrilin AV, Viouchkov YL, Larbalestier DC, Abraimov DV. Progress in the development of a superconducting 32 T magnet with REBCO high field coils. Appl Supercond IEEE Trans Supercond. 2014; 24(3):1–5.
18. Yanagisawa Y, Nakagome H, Hosono M, Hamada M, Kiyoshi T, Hobo F, Takahashi M, Yamazaki T, Maeda H. Towards beyond-1 GHz solution NMR: internal ^{2}H lock operation in an external current mode. J Magn Reson. 2008; 192(2):329–337. [PubMed: 18424127]
19. Nishiyama, Y., Pandey, MK., Florian, P., Fyon, F., Hashi, K., Ohki, S., Nishijima, G., Matsumoto, S., Noguchi, T., Deguchi, T., Gotom, A., Shimizu, T., Maeda, H., Takahashi, M., Yanagisawa, Y., Tanaka, R., Nemoto, T., Miyamoto, T., Suematsu, H., Saito, K., Miki, T. Presented at the 56th experimental nuclear magnetic resonance conference (ENC). Asilomar, CA: 2015. 1020 MHz LTS/HTS NMR: II. Application to solid-state NMR.
20. van der Laan DC, Goodrich LF, Noyes P, Trociewitz UP, Godeke A, Abraimov D, Francis A, Larbalestier DC. Engineering current density in excess of 100 A/mm^{2} at 20 T in CORC magnet cables containing RE-$Ba_2Cu_3O_{7-\delta}$ tapes with 38 m thick substrates. Supercond Sci Technol. 2015; 28:124001. (**p 8**).
21. Godeke D, Cheng D, Dietderich DR, English CD, Felice H, Hannaford CR, Prestemon SO, Sabbi G, Scanlan RM, Hikichi Y, Nishioka J, Hasegawa T. Development of wind-and-React bi-2212 accelerator magnet technology. IEEE Trans Appl Supercond. 2008; 18(2):516–519.
22. Takayasu M, Chiesa L, Allen NC, Minervini JV. Present status and recent development of the twisted stacked-tape cable (TSTC) conductor. IEEE Trans Appl Supercond. 2016
23. Haiying L, Jun Xiao L. Gradient coil mechanical vibration and image quality degradation. Proceedings of the society of magnetic resonance. 1996:1393.

24. Mansfield P, Chapman BL, Bowtell R, Glover P, Coxon R, Harvey PR. Active acoustic screening: reduction of noise in gradient coils by Lorentz force balancing. Magn Reson Med. 1995; 33(2): 276–281. [PubMed: 7707921]
25. Jia F, Schultz G, Testud F, Wetz AM, Weber H, Littin S, Yu H, Hennig J, Zaitsev M. Performance evaluation of matrix gradient coils. MAGMA. 2016; 29(1):59–73. [PubMed: 26667966]
26. Stockmann, JP., Witzel, T., Blau, JN., Polemini, JR., Zhao, W., Keil, B., Wald, LL. Combined Shim RF array for highly efficient shimming of the brain at 7 T; Proceedings of the scientific meeting, International Society for Magnetic Resonance in Medicine; 2013. p. 225
27. Han H, Song AW, Trrung TK. 2013Integrated parallel reception, excitation and shimming (IPRESS). Proceedings of the scientific meeting, International Society for Magnetic Resonance in Medicine. :664.
28. Stockmann JP, Witzel T, Keil B, Polimeni JR, Mareyam A, LaPierre C, Setsompop K, Wald L. A 32-channel combined RF and B_0 shim array for 3T brain imaging. Magn Reson Med. 2015; 75(1): 441–451. [PubMed: 25689977]
29. Sodickson DK, Manning WJ. Simultaneous acquisition of spatial harmonics (SMASH): fast imaging with radiofrequency coil arrays. Magn Reson Med. 1997; 38(4):591–603. [PubMed: 9324327]
30. Vaughan JT, Snyder CJ, DelaBarre LJ, Bolan PJ, Tian J, Bolinger L, Adriany G, Andersen P, Strupp J, Ugurbil K. Whole Body imaging at 7T: preliminary results. Magn Reson Med. 2009; 61(1):244–248. [PubMed: 19097214]
31. Katscher U, Börnert P, Leussler C, Van Den Brink JS. Transmit sense. Magn Reson Med. 2003; 49(1):144–150. [PubMed: 12509830]
32. Setsompop K, Alagappan V, Gagoski BA, Potthast A, Hebrank F, Fontius U, Franz Schmitt F, Wald LL, Adalsteinsson E. Broadband slab selection with B1+ mitigation at 7 T via parallel spectral-spatial excitation. Magn Reson Med. 2009; 61(2):493–500. [PubMed: 19161170]
33. Wiesinger F, de Moortele V, Adriany G, De Zanche N, Ugurbil K, Pruessmann KP. Parallel imaging performance as a function of field strength: an experimental investigation using electrodynamic scaling. Magn Reson Med. 2004; 52(5):953–964. [PubMed: 15508167]
34. Guerin B, Gebhardt M, Serano P, Adalsteinsson E, Hamm M, Pfeuffer J, Nistler J, Wald LL. Comparison of simulated parallel transmit body arrays at 3 T using excitation uniformity, global SAR, local SAR, and power efficiency metrics. Magn Reson Med. 2015; 73(3):1137–1150. [PubMed: 24752979]
35. Grissom WA, Xu D, Kerr AB, Fessler JA, Noll DC. Fast large-tip-angle multidimensional and parallel RF pulse design in MRI. IEEE Trans Med Imaging. 2009; 28(10):1548–1559. [PubMed: 19447704]
36. Padormo F, Beqiri A, Hajnal JV, Malik SJ. Parallel transmission for ultrahigh-field imaging. NMR Biomed. 2015
37. Cloos MA, Wiggins C, Wiggins G, Sodickson D. Plug and play parallel transmission at 7 and 9.4 Tesla based on principles from MR fingerprinting. In: Proceedings of the scientific meeting, International Society for Magnetic Resonance in Medicine. 2014; 21:542.
38. Winter L, Niendorf T. On the electrodynamic constraints and antenna array design for human in vivo MR up to 70 Tesla and EPR up to 3 GHz. Proc Intl Soc Magn Reson Med. 2015; 23:1807.
39. Zaitsev M, Dold C, Sakas G, Hennig J, Speck O. Magnetic resonance imaging of freely moving objects: prospective real-time motion correction using an external optical motion tracking system. Neuroimage. 2006; 31(3):1038–1050. [PubMed: 16600642]
40. Godenschweger F, Kägebein U, Stucht D, Yarach U, Sciarra A, Yakupov R, Lüsebrink F, Schulze P, Speck O. Motion correction in MRI of the brain. Phys Med Biol. 2016; 61(5):R32–R56. [PubMed: 26864183]
41. Chen L, Beckett A, Verma A, Feinberg DA. Dynamics of respiratory and cardiac CSF motion revealed with real-time simultaneous multi-slice EPI velocity phase contrast imaging. Neuroimage. 2015; 122:281–287. [PubMed: 26241682]
42. Stucht D, Danishad KA, Schulze P, Godenschweger F, Zaitsev M, Speck O. Highest resolution in vivo human brain MRI using prospective motion correction. PLoS One. 2015; 10(7):e0133921. [PubMed: 26226146]

43. Hoult DI, Richards R. The signal-to-noise ratio of the nuclear magnetic resonance experiment. J Magn Reson. 1976; 24(1):71–85.
44. Cao Z, Park J, Cho ZÄ, Collins CM. Numerical evaluation of image homogeneity, signal-to-noise ratio, and specific absorption rate for human brain imaging at 1.5, 3, 7, 10.5, and 14 T in an 8-channel transmit/receive array. J Magn Reson Imaging. 2015; 41(5):1432–1439. [PubMed: 24976608]
45. Schepkin VD. Sodium MRI of glioma in animal models at ultrahigh magnetic fields. NMR Biomed. 2016; 29(2):175–186. [PubMed: 26174529]
46. Turner R. How much cortex can a vein drain? Downstream dilution of activation-related cerebral blood oxygenation changes. Neuroimage. 2002; 16(4):1062–1067. [PubMed: 12202093]
47. Yacoub E, Harel N, Uğurbil K. High-field fMRI unveils orientation columns in humans. Proc Natl Acad Sci. 2008; 105(30):10607–10612. [PubMed: 18641121]
48. Zimmermann J, Goebel R, De Martino F, van de Moortele P-F, Feinberg D, Adriany G, Chaimow D, Shmuel D, Uğurbil K, Yacoub E. Mapping the organization of axis of motion selective features in human area MT using high-field fMRI. PLoS One. 2011; 6(12):e28716. [PubMed: 22163328]
49. De Martino F, Moerel M, Ugurbil K, Goebel R, Yacoub E, Formisano E. Frequency preference and attention effects across cortical depths in the human primary cortex. Proc Natl Acad Sci USA. 2015; 112:16036–16041. [PubMed: 26668397]
50. Muckli L, De Martino F, Vizoli L, Petro LS, Smith FW, Ugurbil K, Goebel R, Yacoub E. Contextural feedback to superficial layers of V1. Curr Biol. 2015; 25:2690–2695. [PubMed: 26441356]
51. Olman CA, Harel N, Feinberg DA, He S, Zang P, Ugurbil K, Yacoub E. Layer-specific fMRI reflects different neuronal computations at different depths in human V1. PLoS One. 2012; 7:e332536.
52. Nasr S, Polimeni JR, Tootell RB. Interdigitated color-and disparity-selective columns within human visual cortical areas V2 and V3. J Neurosci. 2016; 36(6):1841–1857. [PubMed: 26865609]
53. Heidemann RM, Anwander A, Feiweier T, Knösche TR, Turner R. k-space and q-space: combining ultra-high spatial and angular resolution in diffusion imaging using ZOOPPA at 7T. Neuroimage. 2012; 60(2):967–978. [PubMed: 22245337]
54. Gorgolewski KJ, Mendes N, Wilfling D, Wladimirow E, Gauthier CJ, Bonnen T, Ruby FJ, Trampel R, Bazin PL, Cozatl R, Smallwood J, Margulies DS. A high resolution 7-Tesla resting-state fMRI test-retest dataset with cognitive and physiological measures. Sci Data. 2015; 2:140054. [PubMed: 25977805]
55. Goa PE, Koopmans PJ, Poser BA, Barth M, Norris DG. BOLD fMRI signal characteristics of S1- and S2-SSFP at 7 Tesla. Front Neurosci. 2014; 8:49. [PubMed: 24659952]
56. Setsompop K, Feinberg DA, Polimeni JR. Rapid brain MRI acquisition techniques at ultra-high fields. NMR Biomed. 2016
57. Basser PJ, Pierpaoli C. Microstructural and physiological features of tissues elucidated by quantitative-diffusion-tensor MRI. J Magn Reson. 2011; 213(2):560–570. [PubMed: 22152371]
58. Jones DK, Knösche TR, Turner R. White matter integrity, fiber count, and other fallacies: the do's and don'ts of diffusion MRI. Neuroimage. 2013; 73:239–254. [PubMed: 22846632]
59. Tuch DS, Reese TG, Wiegell MR, Makris N, Belliveau JW, Wedeen VJ. High angular resolution diffusion imaging reveals intravoxel white matter fiber heterogeneity. Magn Reson Med. 2002; 48(4):577–582. [PubMed: 12353272]
60. Vu A, Auerbach E, Lenglet C, Moeller S, Sotiropoulos SN, Jbabdi S, Andersson J, Yacoub E, Ugurbil K. High resolution whole brain diffusion imaging at 7T for the human connectome project. Neuroimage. 2015; 122:318–331. [PubMed: 26260428]
61. Ford AA, Colon-Perez L, Triplett WT, Gullett JM, Mareci TH, FitzGerald DB. Imaging white matter in human brain-stem. Front Hum Neurosci. 2013; 7:400. [PubMed: 23898254]
62. Colon-Perez LM, King M, Parekh M, Boutzoukas A, Carmona E, Couret M, Klassen R, Mareci TH, Carney PR. High-field magnetic resonance imaging of the human temporal lobe. Neuroimage Clin. 2015; 9:58–68. [PubMed: 26413472]

63. Leuze CW, Anwander A, Bazin PL, Dhital B, Stüber C, Reimann K, Geyer S, Turner R. Layer-specific intracortical connectivity revealed with diffusion MRI. Cereb Cortex. 2014; 24(2):328–339. [PubMed: 23099298]
64. Shemesh N, Dumez JÄ, Frydman L. Longitudinal relaxation enhancement in 1H NMR spectroscopy of tissue metabolites via spectrally selective excitation. Chem A Eur J. 2013; 19(39): 13002–13008.
65. Guivel-Scharen V, Sinnwell T, Wolff SD, Balaban RS. Detection of proton chemical exchange between metabolites and water in biological tissues. J Magn Reson. 1998; 133(1):36–45. 49. [PubMed: 9654466]
66. Jones CK, Polders D, Hua J, Hoogduin HJ, Zhou J, van Zijl PCM. In Vivo 3D whole-brain pulsed steady state chemical exchange saturation transfer at 7T. Magn Reson Med. 2012; 67(6):1579–1589. [PubMed: 22083645]
67. Van Zijl P, Yadav N. Chemical exchange saturation transfer (CEST): what is in a name and what isn't? Magn Reson Med. 2011; 65(4):927–948. [PubMed: 21337419]
68. Jones CK, Huang A, Xu J, Edden RA, Schär M, Hua J, Oskolkov N, Zacà D, Zhou J, McMahon MT, Pillai JJ, van Zijl PC. Nuclear overhauser enhancement (NOE) imaging in the human brain at 7T. Neuroimage. 2013; 77:114–124. [PubMed: 23567889]
69. Lu A, Atkinson IC, Zhou XJ, Thulborn KR. PCr/ATP ratio mapping of the human head by simultaneously imaging of multiple spectral peaks with interleaved excitations and flexible twisted projection imaging readout trajectories at 9.4 T. Magn Reson Med. 2013; 69(2):538–544. [PubMed: 22529019]
70. Zhu, X., Du, F., Zhang, N., Zhang, Y., Lei, H., Zhang, X., Qiao, H., Uğurbil, K., Chen, W. Advanced in vivo heteronuclear MRS approaches for studying brain bioenergetics driven by Mitochondria. In: Hyder, F., editor. Dynamic brain imaging: multimodal methods and in vivo applications. Humana Press; New York: 2009. p. 317-357.
71. Rooney WD, Li X, Sammi MK, Bourdette DN, Neuwelt EA, Springer CS. Mapping human brain capillary water lifetime: high-resolution metabolic neuroimaging. NMR Biomed. 2015; 28(6):607–623. [PubMed: 25914365]
72. Springer CS, Li X, Tudorica LA, Oh N, Roy SY-C, Chui AM, Naik ML, Holtorf ML, Afzala A, Rooney WD, Huang W. Intratumor mapping of intracellular water lifetime: metabolic images of breast cancer? NMR Biomed. 2014; 27(7):760–773. [PubMed: 24798066]
73. Rooney, WD., Sammi, MK., Grinstead, JW., Pollaro, J., Selzer, A., Li, X., Springer, CS. Contrast reagent detection sensitivity increases with B_0: 3T and 7T comparison of the human head; Proceedings of the International Society for Magnetic Resonance in Medicine; 2013. p. 1224
74. Rooney WD, Johnson G, Li X, Cohen ER, Kim S-G, Uğurbil K, Springer CS. Magnetic field and tissue dependences of human brain longitudinal ^1H_2O relaxation in vivo. Magn Reson Med. 2007; 57:308–318. [PubMed: 17260370]
75. Kiyatkin EA, Lenoir M. Rapid fluctuations in extracellular brain glucose levels induced by natural arousing stimuli and intravenous cocaine: fueling the brain during neural activation. J Neurophysiol. 2012; 108(6):1669–1684. [PubMed: 22723672]
76. Valvassori SS, Calixto KV, Budni J, Resende WR, Varela RB, de Freitas KV, Gonçalves CL, Streck EL, Quevedo J. Sodium butyrate reverses the inhibition of Krebs cycle enzymes induced by amphetamine in the rat brain. J Neural Transmis. 2013; 120(12):1737–1742.
77. Lu A, Atkinson IC, Claiborne TC, Damen FC, Thulborn KR. Quantitative sodium imaging with a flexible twisted projection pulse sequence. Magn Reson Med. 2010; 63(6):1583–1593. [PubMed: 20512862]
78. Thulborn KR, Lui E, Guntin J, Jamil S, Sun Z, Claiborne T, Atkinson IC. Quantitative sodium MR imaging of the human brain at 9.4 Tesla provides assessment of tissue sodium concentration and cell volume fraction during normal ageing. Invited submission to special edition. NMR Biomed. 2016; 29:137–143. [PubMed: 26058461]
79. Thulborn KR, Lu A, Atkinson IC, Damen F, Villano JL. Quantitative sodium MR imaging and sodium bioscales for the management of brain tumors. Neuroimaging Clin N Am. 2009; 19(4): 615–624. [PubMed: 19959008]

80. Qian Y, Zhao T, Zheng H, Weimer J, Boada FE. High-resolution sodium imaging of human brain at 7 T. Magn Reson Med. 2012; 68(1):227–233. [PubMed: 22144258]
81. Fleysher L, Oesingmann N, Brown R, Sodickson DK, Wiggins GC, Inglese M. Noninvasive quantification of intracel-lular sodium in human brain using ultrahigh-field MRI. NMR Biomed. 2013; 26(1):9–19. [PubMed: 22714793]
82. Umathum R, Rösler MB, Nagel AM. In vivo ^{39}K MR imaging of human muscle and brain. Radiology. 2013; 269(2):569–576. [PubMed: 23878285]
83. Atkinson IC, Claiborne TC, Thulborn KR. Feasibility of 39-potassium MR imaging of a human brain at 9.4 Tesla. Magn Reson Med. 2014; 71(5):1819–1825. [PubMed: 23798343]
84. Nagel AM, Lehmann-Horn F, Weber M-A, Jurkat-Rott K, Wolf MB, Radbruch A, Umathum R, Semmler W. In vivo ^{35}Cl MR imaging in humans: a feasibility study. Radiology. 2014; 271(2): 585–595. [PubMed: 24495267]
85. Schepkin VD, Choy IO, Budinger TF, Obayashi DY, Taylor SE, DeCampli WM, Amartur SC, Young JN. Sodium TQF NMR and intracellular sodium in isolated crystalloid perfused rat heart. Magn Reson Med. 1998; 39(4):557–563. [PubMed: 9543417]
86. Schepkin VD, Odintsov BM, Litvak I, Gor'kov PL, Brey WW, Neubauer A, Budinger TF. Efficient detection of bound potassium and sodium using TQTPPI pulse sequence. Proceedings of the scientific meeting, International Society for Magnetic Resonance in Medicine. 2015; 23:2375.
87. Zhu XÄ, Zhang N, Zhang Y, Zhang X, Ugurbil K, Chen W. In vivo ^{17}O NMR approaches for brain study at high field. NMR Biomed. 2005; 18(2):83–103. [PubMed: 15770611]
88. Atkinson IC, Thulborn KR. Feasibility of mapping the tissue mass corrected bioscale of cerebral metabolic rate of oxygen consumption using 17-oxygen and 23-sodium MR imaging in a human brain at 9.4 T. Neuroimage. 2010; 51(2):723–733. [PubMed: 20188194]
89. Katscher U, Voigt T, Findeklee C, Vernickel P, Nehrke K, Dossel O. Determination of electric conductivity and local SAR via B1 mapping. IEEE Trans Med Imaging. 2009; 28(9):1365–1374. [PubMed: 19369153]
90. van Lier AL, Brunner DO, Pruessmann KP, Klomp DW, Luijten PR, Lagendijk JJ, van den Berg CA. B_1+ Phase mapping at 7 T and its application for in vivo electrical conductivity mapping. Magn Reson Med. 2012; 67(2):552–561. [PubMed: 21710613]
91. van Lier AL, Raaijmakers A, Voigt T, Lagendijk JJW, Leijten PR, Katscher U, van den Berg CAT. Electrical properties tomography in the human brain at 1.5, 3, and 7 T: a comparison study magnetic resonance in medicine. Magn Reson Med. 2014; 71:354–363. [PubMed: 23401276]
92. Liu J, Zhang X, Van de Moortele P-F, Schmitter S, He B. Determining electrical properties based on B1 fields measured in an MR scanner using a multi-channel transmit/receive coil: a general approach. Phys Med Biol. 2013; 58(13):4395. [PubMed: 23743673]
93. Sodickson, DK., Alon, L., Deniz, CM., Ben-Eliezer, N., Cloos, M., Sodickson, LA., Collins, CM., Wiggins, GC., Novikov, DS. Proceedings of the 21st annual meeting of ISMRM. Salt Lake City, Utah: 2013. Generalized local Maxwell tomography for mapping of electrical property gradients and tensors; p. 417575
94. Budinger TF. Nuclear magnetic resonance (NMR) in vivo studies: known thresholds for health effects. J Comput Assist Tomogr. 1981; 5:800–811. [PubMed: 7033311]
95. Schenck JF. Health and physiological effects of human exposure to whole-body four-tesla magnetic fields during MRI. Ann NY Acad Sci. 1992; 649(1):285–301. [PubMed: 1580500]
96. National Research Council. Current Status and future direction of high magnetic field science in the United States. National Academies Press; Washington, DC, Appendix F: 2013. p. 196-206.
97. Vaughan T, DelaBarre L, Snyder C, Tian J, Akgun C, Shrivastava D, Liu W, Olson C, Adriany G, Strupp J, Andersen P, Gopi-nath A, van de Moortele PF, Garwood M, Ugurbil K. 9.4 T human MRI: preliminary results. Magn Reson Med. 2006; 56(6):1274–1282. [PubMed: 17075852]
98. Atkinson IC, Sonstegaard R, Pliskin NH, Thulborn KR. Vital signs and cognitive function are not affected by 23-sodium and 17-oxygen magnetic resonance imaging of the human brain at 9.4 T. J Magn Reson Imaging. 2010; 32(1):82–87. [PubMed: 20578014]
99. Chakeres DW, Kangarlu A, Boudoulas H, Young DC. Effect of static magnetic field exposure of up to 8 tesla on sequential human vital sign measurements. J Magn Reson Imaging. 2003; 18:346–352. [PubMed: 12938131]

100. Atkinson, IC., Renteria, L., Holly Burd, H., Neil, H., Pliskin, NH., Thulborn, KR. Safety of human MRI at static fields above the FDA 8T guideline: sodium imaging at 9.4T does not affect vital signs or cognitive ability (2015) Online access December 2015. 2015. http://indigo.uic.edu/bitstream/handle/10027/7232/94THumanSafety_prepress.pdf
101. Budinger TF, Fischer H, Hentschel D, Reinfelder H-E, Schmitt F. Physiological effects of fast oscillating magnetic field gradients. J Comput Assist Tomogr. 1991; 15(6):909–914. [PubMed: 1939767]
102. Schenck JF. Safety of strong, static magnetic fields. J Magn Reson Imaging. 2000; 12(1):2–19. [PubMed: 10931560]
103. Houpt TA, Pittman DW, Barranco JM, Brooks EH, Smith JC. Behavioral effects of high-strength static magnetic fields on rats. J Neurosci. 2003; 23(4):1498–1505. [PubMed: 12598638]
104. Houpt TA, Cassell JA, Riccardi C, DenBleyker MD, Hood A, Smith JC. Rats avoid high magnetic fields: dependence on an intact vestibular system. Physiol Behav. 2007; 92(4):741–747. [PubMed: 17585969]
105. Kirschvink JL, Kobayashi-Kirschvink A, Woodford BJ. Magnetite biomineralization in the human brain. Proc Natl Acad Sci USA. 1992; 89:7683–7687. [PubMed: 1502184]
106. Budinger TF, Glaeser RM. Measurement of focus and spherical abberation of an electron microscope objective lens. Ultramicroscopy. 1977; 2:31–41.
107. Hong FT. Magnetic field effects on biomolecules, cells, and living organisms. Biosystems. 1995; 36(3):187–229. [PubMed: 8573700]
108. Fukunaga M, Li T-Q, van Gelderen P, de Zwart JA, Shmueli K, Yao B, Lee J, Maric D, Aronova MA, Zhang G, Leapman RD, Schenck JF, Merkle H, Duyn JH. Layer-specific variation of iron content in cerebral cortex as a source of MRI contrast. Proc Natl Acad Sci USA. 2010; 107(8): 3834–3839. [PubMed: 20133720]
109. Schenck JF. The role of magnetic susceptibility in magnetic resonance imaging: MRI magnetic compatibility of the first and second kinds. Med Phys. 1996; 23(6):815–850. [PubMed: 8798169]
110. Berry MV, Geim AK. Of flying frogs and levitrons. Eur J Phys. 1997; 18:307–313.
111. Roth BJ, Basser PJ. Mechanical model of neural tissue displacement during Lorentz effect imaging. Magn Reson Med. 2009; 61:59–64. [PubMed: 19097218]
112. Wikswo JP, Barach JP. An estimate of the steady magnetic field strength required to influence nerve conduction. IEEE Trans Biomed Eng. 1980; 27(12):722–723. [PubMed: 7461647]
113. Tenforde TS. Magnetically induced electric fields and currents in the circulatory system. Prog Biophys Mol Biol. 2005; 87(2):279–288. [PubMed: 15556666]
114. d'Arsonval A. Dispositifs pour la mesure des courants alternatifs de toutes fréquences. C R Soc Biol (Paris). 1896; 2:450–451.
115. Lövsund P, Őberg PA, Nilsson SEG. Magnetophosphenes: a quantitative analysis of thresholds. Med Biol Eng Comput. 1980; 18(3):326–334. [PubMed: 6968384]
116. Keltner JR, Roos MS, Brakeman PR, Budinger TF. Magnetohydrodynamics of blood flow. Magn Reson Med. 1990; 16(1):139–149. [PubMed: 2255234]
117. Weiss J, Herrick RC, Taber KH, Contant C, Plishker GA. Bio-effects of high magnetic fields: a study using a simple animal model. Magn Reson Imaging. 1992; 10(4):689–694. [PubMed: 1501539]
118. Patel M, Williamsom RA, Dorevitch S, Buchanan S. Pilot study investigating the effect of the static magnetic field from a 9.4-T MRI on the vestibular system. J Occup Environ Med. 2008; 50(5):576–583. [PubMed: 18469627]
119. Theysohn JM, Maderwald S, Kraff O, Moenninghoff C, Ladd ME, Ladd SC. Subjective acceptance of 7 Tesla MRI for human imaging. Magn Reson Mater Phys Biol Med. 2008; 21(1–2):63–7294.
120. Glover P, Cavin I, Qian W, Bowtell R, Gowland P. Magnetic-field-induced vertigo: a theoretical and experimental investigation. Bioelectromagnetics. 2007; 28(5):349–361. [PubMed: 17427890]
121. van Nierop LEV, Slottje P, Zandvort MJV, De Vocht F, Kromhout H. Effects of magnetic stray fields from a 7 Tesla MRI scanner on neurocognition: a double-blind randomised crossover study. Occup Environ Med. 2012; 69(10):761–768.

122. Cason AM, Kwon B, Smith JC, Houpt TA. Labyrinthectomy abolishes the behavioral and neural response of rats to a high-strength static magnetic field. Physiol Behav. 2009; 97(1):36–43. [PubMed: 19419674]

123. Roberts DC, Marcelli V, Gillen JS, Carey JP, Della Santina CC, Zee DS. MRI magnetic field stimulates rotational sensors of the brain. Curr Biol. 2011; 21(19):1635–1640. [PubMed: 21945276]

124. Kassemi M, Deserranno D, Oas J. Fluid-structural interactions in the inner ear. Comput Struct. 2005; 83(2):181–189.

125. Mian OS, Li Y, Antunes A, Glover PM, Day BL. Effect of head pitch and roll orientations on magnetically induced vertigo. J Physiol. 2016; 594(4):1051–1067. [PubMed: 26614577]

126. Wolff S, Crooks LE, Brown P, Howard R, Painter RB. Tests for DNA and chromosomal damage induced by nuclear magnetic resonance imaging. Radiology. 1980; 136(3):707–710. [PubMed: 7403551]

127. Okano H. Effects of static magnetic fields in biology: role of free radicals. Front Biosci. 2008; 13:6106–6125. [PubMed: 18508647]

128. Schenck JF. Physical interactions of static magnetic fields with living tissues. Progr Biophys Molecular Biol. 2005; 87(2–3):185–204.

129. Miyakoshi J. Effects of static magnetic fields relevant to human health. Progr Biophys Molecular Biol. 2005; 87(2–3):213–223.

130. Vijayalaxmi FM, Speck O. Magnetic resonance imaging (MRI): a review of genetic damage investigations. Mutat Res. 2015; 764:51–63.

131. Bras W, Diakun GP, Díaz JF, Maret G, Kramer H, Bordas J, Medrano FJ. The susceptibility of pure tubulin to high magnetic fields: a magnetic birefringence and X-ray fiber diffraction study. Biophys J. 1998; 74:1509–1521. [PubMed: 9512047]

132. Denegre JM, Valles JM Jr, Lin K, Jordan WB, Mowry KL. Cleavage planes in frog eggs are altered by strong magnetic fields. Proc Natl Acad Sci USA. 1998; 95(25):14729–14732. [PubMed: 9843957]

133. Valiron O, Peris L, Rikken G, Schweitzer A, Saoudi Y, Remy C, Job D. Cellular disorders induced by high magnetic fields. J Magn Reson Imaging. 2005; 22(3):334–340. [PubMed: 16106367]

134. Cai R, Yang H, He J, Zhu W. The effects of magnetic fields on water molecular hydrogen bonds. J Molecular Struct. 2009; 938:15–19.

135. Paul A-L, Ferl RJ, Meisel MW. High magnetic field induced changes of gene expression in *Arabidopsis*. BioMagn Res Technol. 2006; 4:7. [PubMed: 17187667]

136. Brand M, Ellmann S, Sommer M, May MS, Eller A, Wuest W, Engert C, Achenbach S, Kuefner MA, Baeuerle T, Lell M, Uder M. Influence of cardiac MR imaging on DNA double-strand breaks in human blood lymphocytes. Radiology. 2015; 277(2):406–412. [PubMed: 26225451]

137. Reddig A, Fatahi M, Friebe B, Guttek K, Hartig R, Goden-schweger F, Roggenbuck D, Ricke J, Reinhold D, Speck O. Analysis of DNA double-strand breaks and cytotoxicity after 7 Tesla magnetic resonance imaging of isolated human lymphocytes. PLoS One. 2015; 10(7):e0132702. (eCollection 2015). [PubMed: 26176601]

138. Fatahi M, Reddig A, Vijayalaxmi Friebe B, Hartig R, Prihoda TJ, Ricke J, Roggenbuck D, Reinhold D, Speck O. DNA double-strand breaks and micronuclei in human blood lymphocytes after repeated whole body exposures to 7T Magnetic Resonance Imaging. Neuroimage. 2016

139. Giovannelli L, Pitozzi V, Moretti S, Boddi V, Dolara P. Seasonal variations of DNA damage in human lymphocytes: correlation with different environmental variables. Mutat Res. 2006; 593(1–2):143–152. [PubMed: 16095632]

140. Télez M, Ortiz-Lastra E, Gonzalez AJ, Flores P, Huerta I, Ramírez JM, Barasoain M, Criado B, Arrieta I. Assessment of the genotoxicity of atenolol in human peripheral blood lymphocytes: correlation between chromosomal fragility and content of micronuclei. Mutat Res. 2010; 695(1–2):46–54. [PubMed: 19932191]

141. Vilenchik MM, Knudson AG. Endogenous DNA doublestrand breaks: production, fidelity or repair, and induction of cancer. Proc Natl Acad Sci. 2003; 100(22):12871–12876. [PubMed: 14566050]

142. Winter L, Oezerdem C, Hoffmann W, van de Lindt T, Periquito J, Ji Y, Ghadjar P, Budach V, Wust P, Niendorf T. Thermal magnetic resonance: physics considerations and electromagnetic field simulations up to 23.5 Tesla (1 GHz). Radiat Oncol. 2015; 10:201. [PubMed: 26391138]

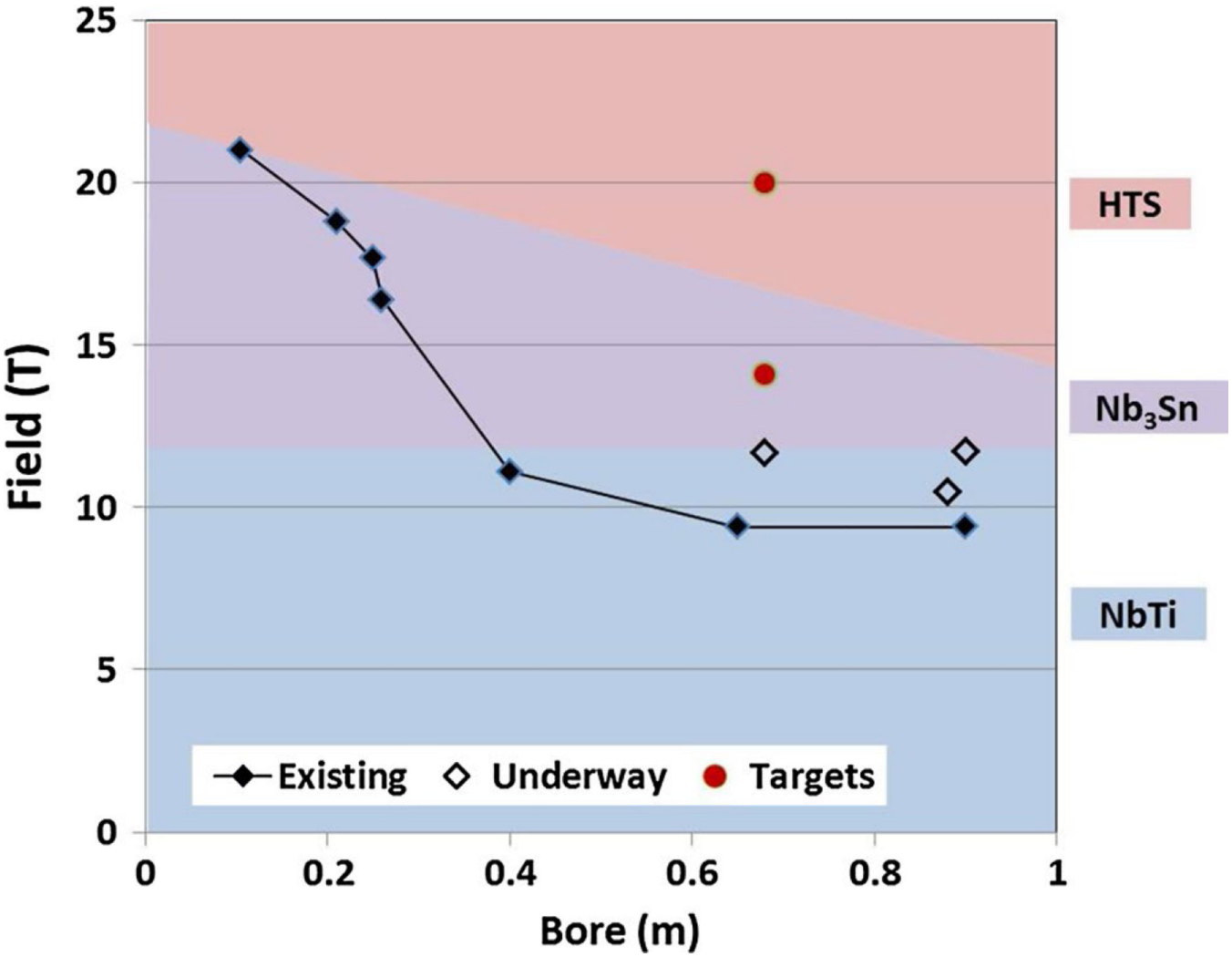

Fig. 1.

Existing magnets and projects are shown with the required conductor. *Solid diamonds* indicate magnets presently in operation. *Open diamonds* indicate magnets presently under construction or repair. Target magnet designs in this paper are shown as *red circles*

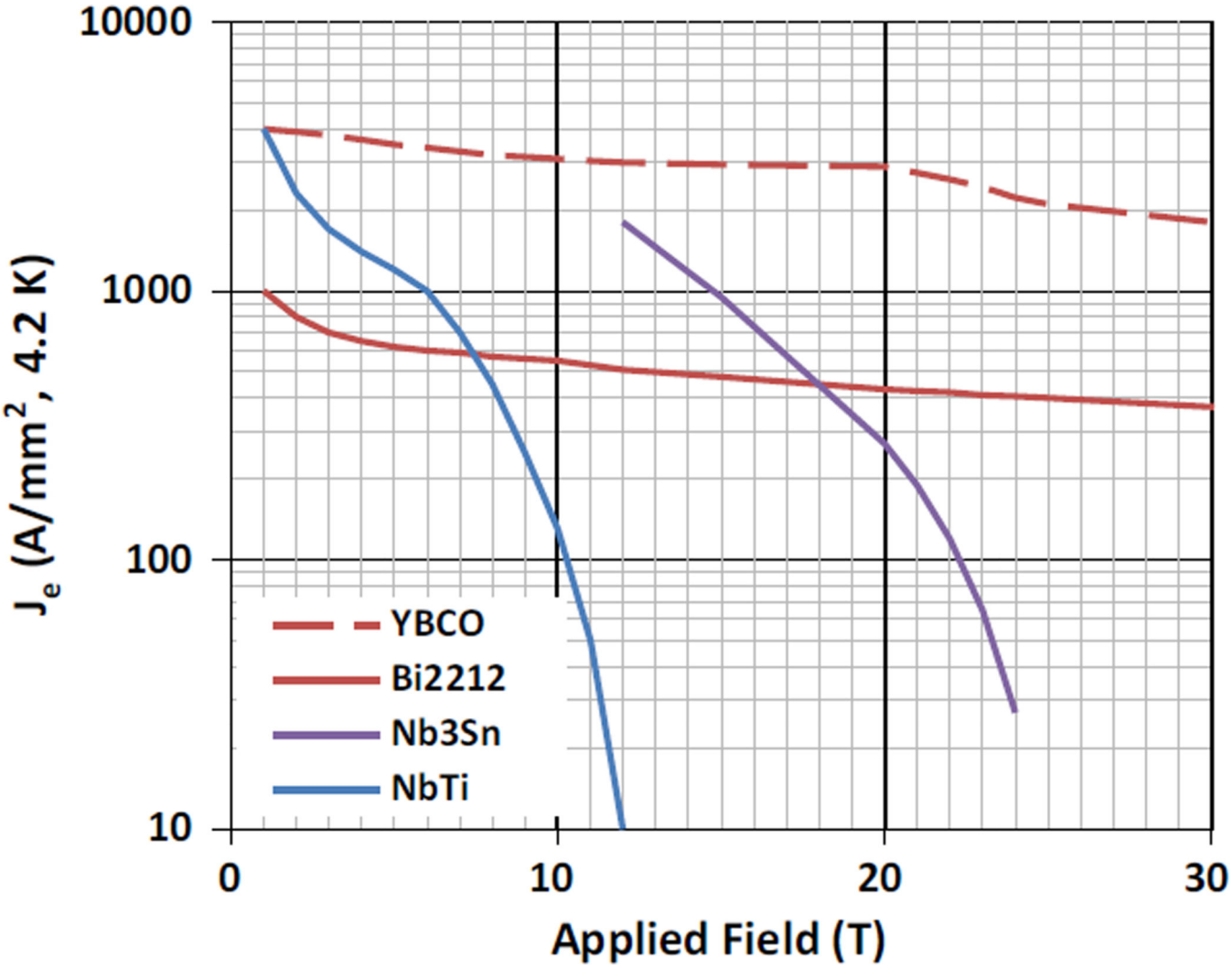

Fig. 2.

Maximum current density of superconducting wires as a function of the applied magnetic field. The *curve* for Nb_3Ti illustrates the feasibility of building a large-bore magnet with a field of 14 T and higher

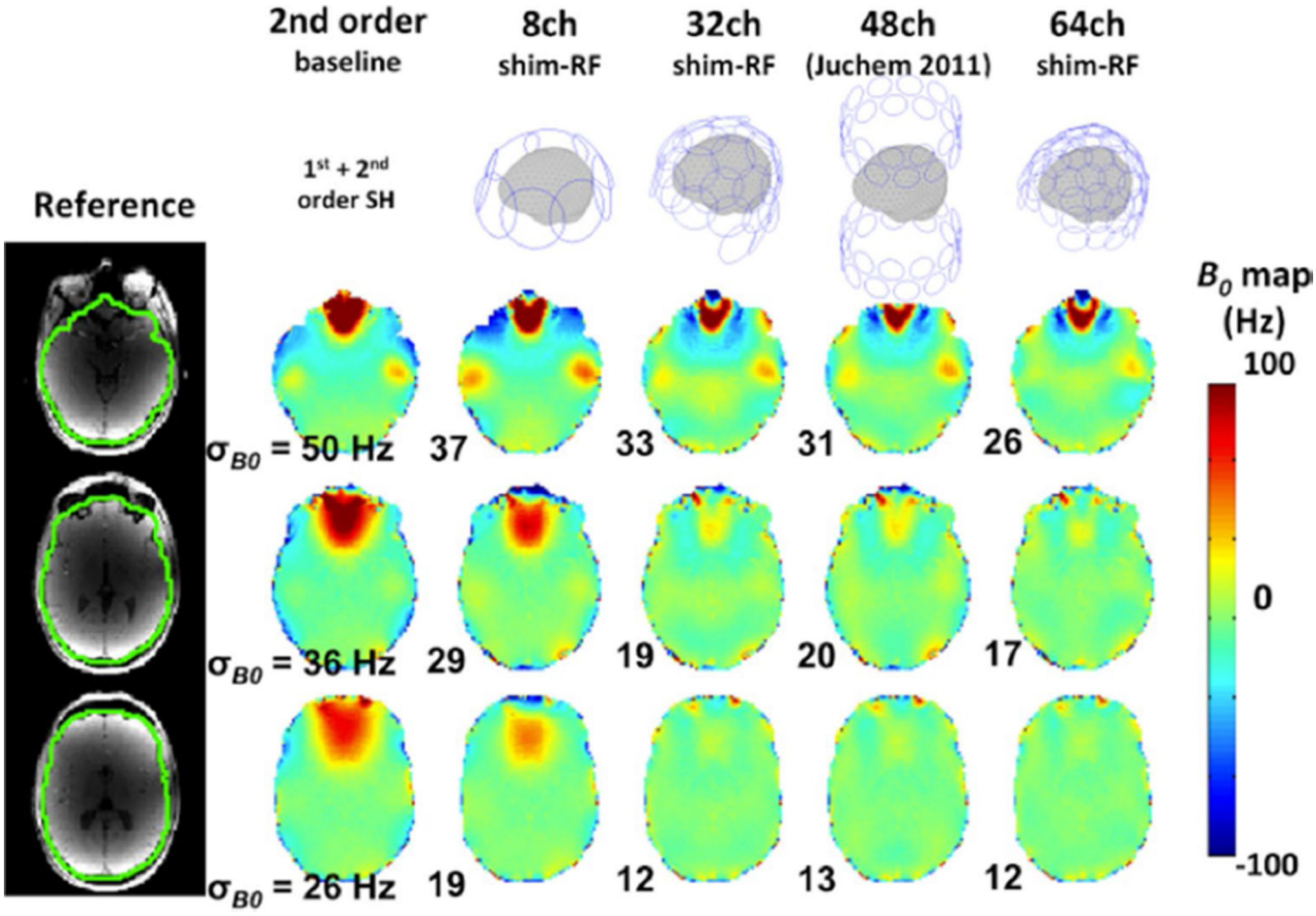

Fig. 3.

Axial field maps through the brain acquired at 3T after shimming with conventional 1st- and 2nd-order Spherical Harmonic (SH) shims. Estimated residual patterns after shimming with the Biot-Savart modeled matrix shim array field configurations (8ch, 32ch, 48ch and 64ch). Figure courtesy of Jason Stockmann, MGH

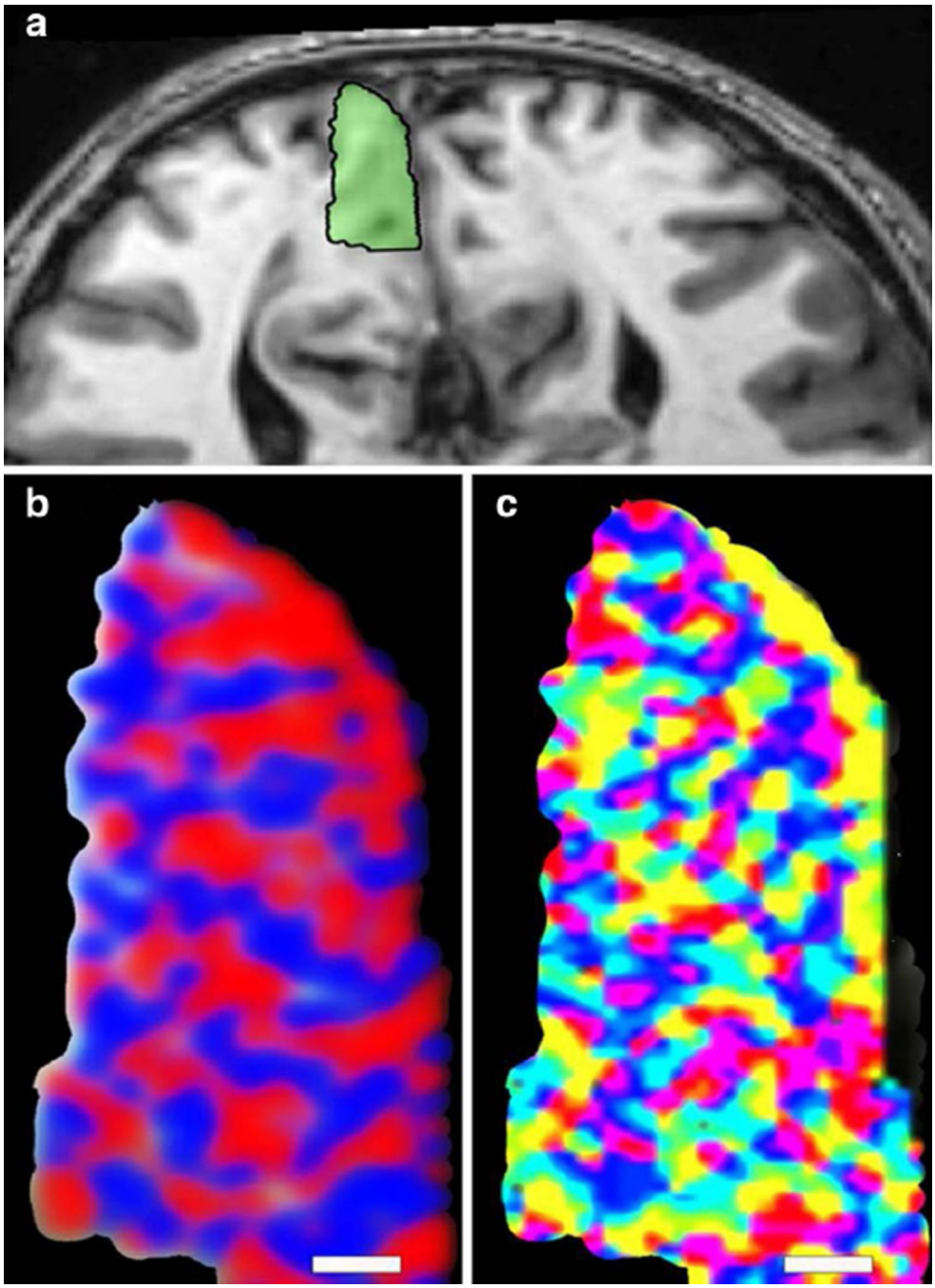

Fig. 4.

Functional columns identified in visual cortical layers by 7 T fMRI. The functional maps in **b** and **c** are enlarged views of the region of interests shown in **a**. The *red* and *blue colors* in **b** indicate preferences to *right* or *left* eye stimulation, whereas the color distribution in **c** represents a given voxel's fMRI time-course phase, which is indicative of its preferred stimulus orientation (*scale bar* 1.0 mm) (University of Minnesota group [47])

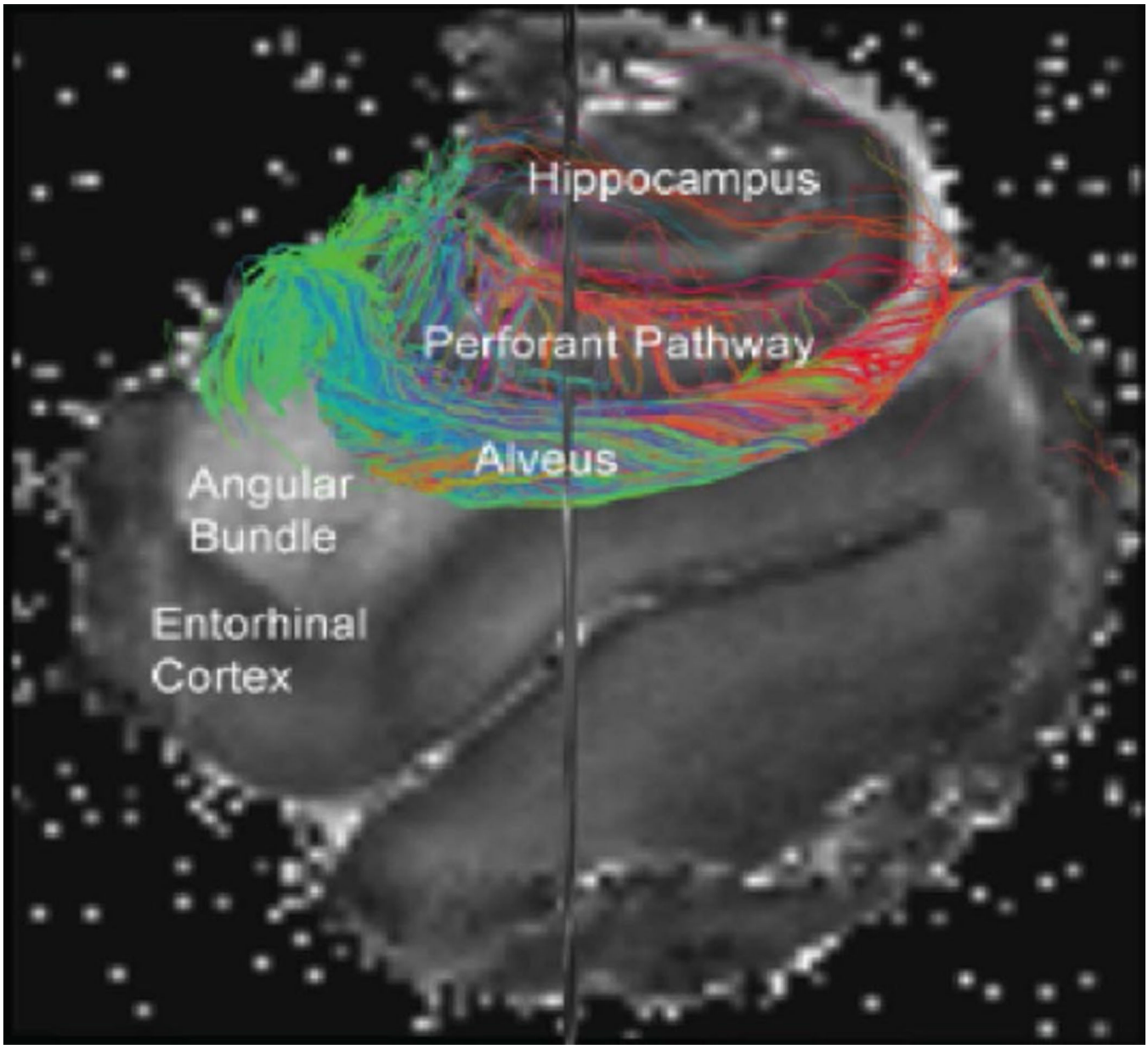

Fig. 5.

DWI tractography data superposed on a proton image obtained at 17.6 T from a freshly excised human hippocampus obtained from epilepsy surgery (University of Florida at Gainesville group)

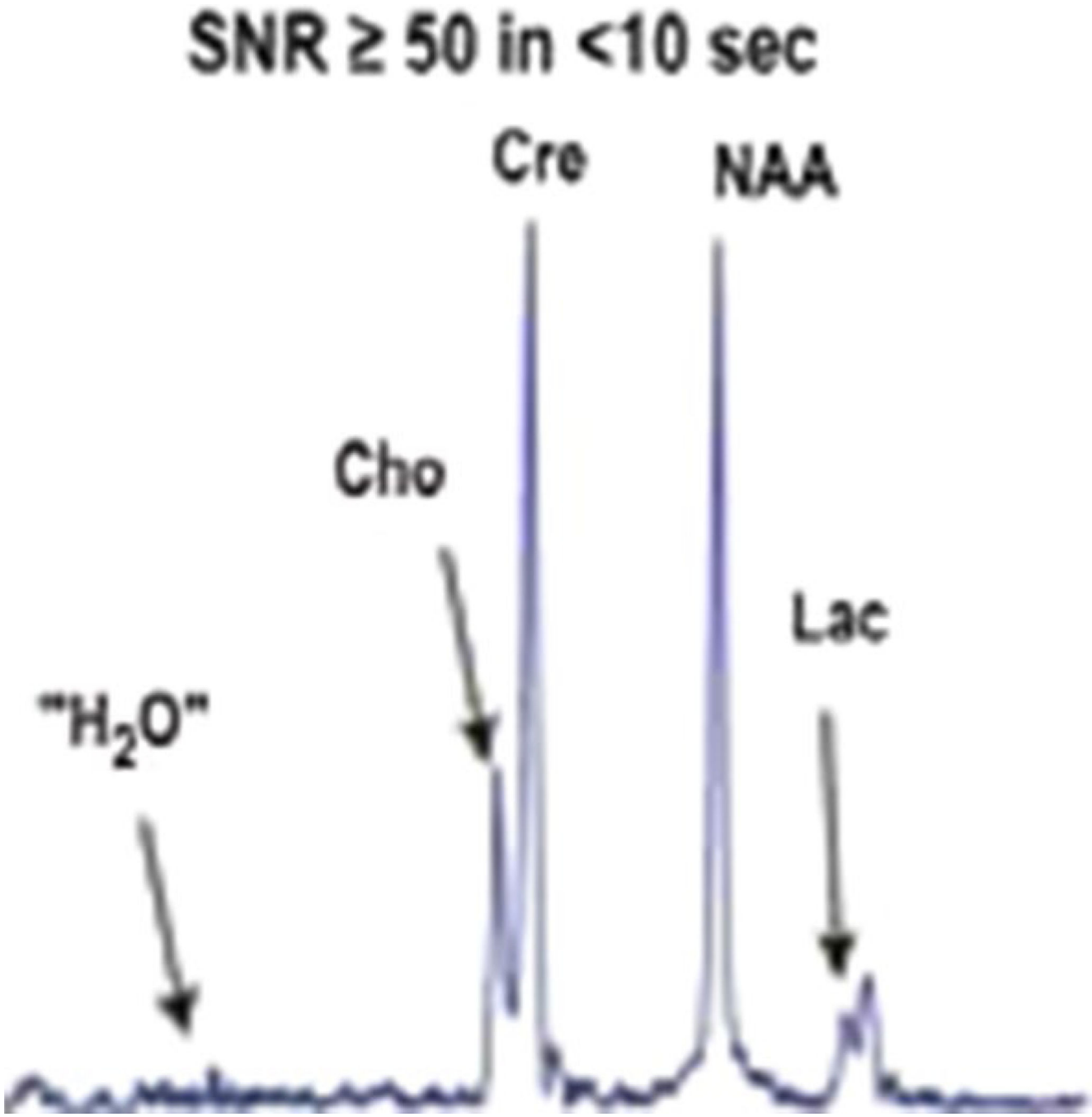

Fig. 6.

Ultrahigh-field (21.1 T) ^{1}H MRS on a 125-μL cubic voxel in the living rodent brain. 1H MRS trace shows choline, creatine, *N*-acetylaspartate, and lactate. The SNR is >50 after 6 s signal averaging. Notice the fat baseline and nearly complete absence of H_2O

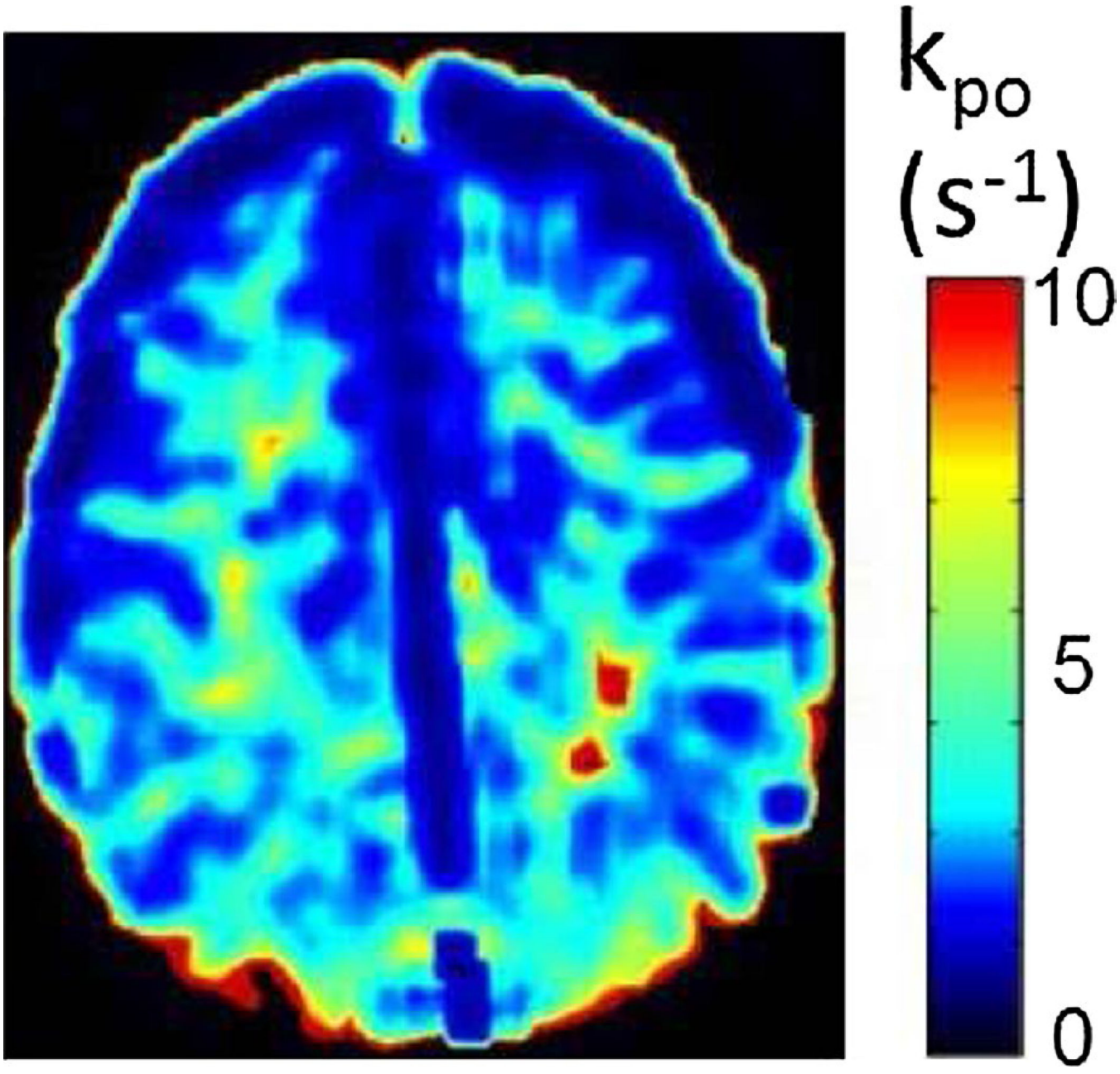

Fig. 7.

Parametric image that reflects NKA kinetics in the normal brain. k_{po} is the inverse of inter-capillary water turnover. The hot spots may reflect WM tracts connecting cortical “rich club nodes,” which participate in many different transient resting-state functional circuits

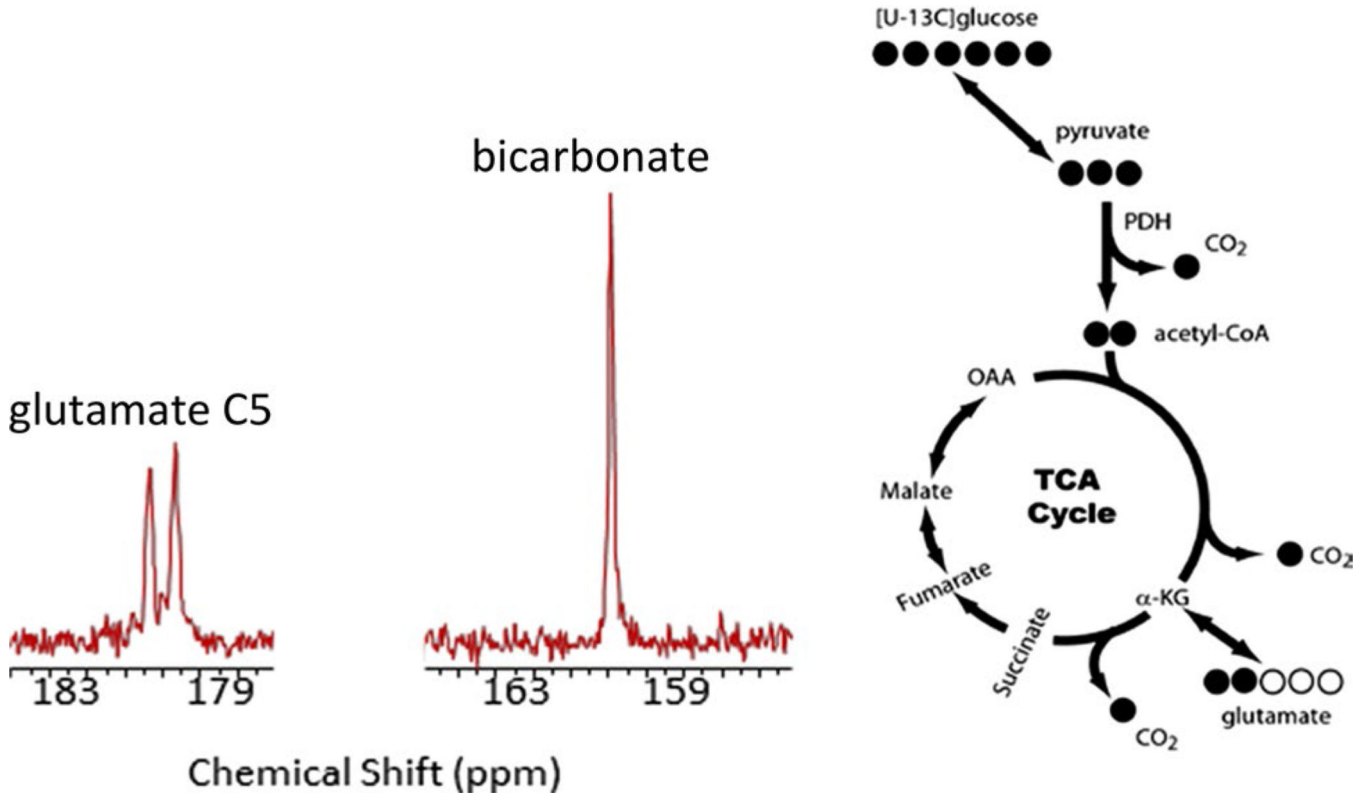

Fig. 8.

^{13}C MRS spectrum of human brain collected in 5 min at 7 T (unlocalized) after i.v. infusion of [U-^{13}C]glucose for 2 h. The spectrum was collected without proton decoupling. *Solid circles* denote labeled carbon (University of Texas Southwestern group)

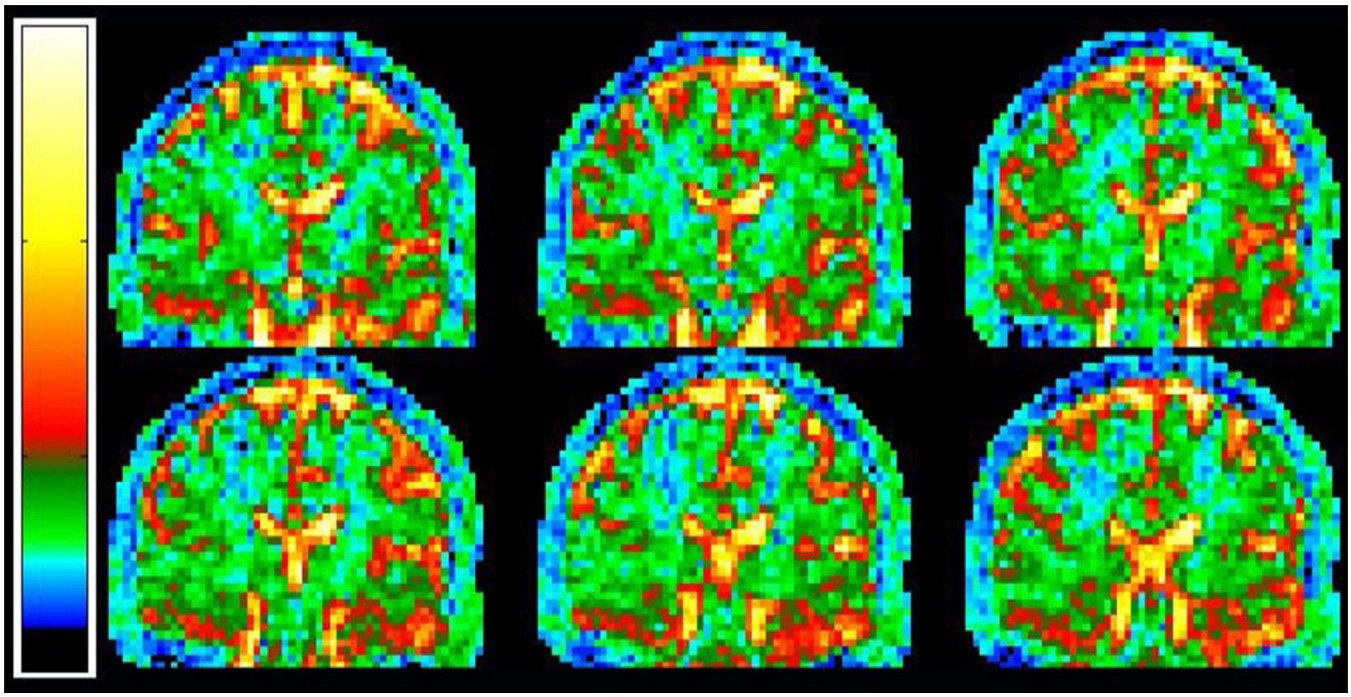

Fig. 9.

Six coronal partitions (2.5-mm contiguous slices) moving from anterior to posterior locations through the lateral ventricles and mesiotemporal regions from a 3D dataset of tissue sodium concentration in the normal adult male brain obtained at 9.4 T with quantitative ^{23}Na MRI. Nominal isotropic resolution is 2.5 mm for a 10-min acquisition. *Color scale* (*left*) is from 0 (*black*) to 150 mM (*white*). The *green* regions have concentrations of 35 ± 3 mM Na, corresponding to a cell volume fraction CVF = 0.81 ± 0.2. Cerebrospinal fluid (CSF) has a concentration of 145 mM corresponding to the *yellow-white* end of the *color scale*

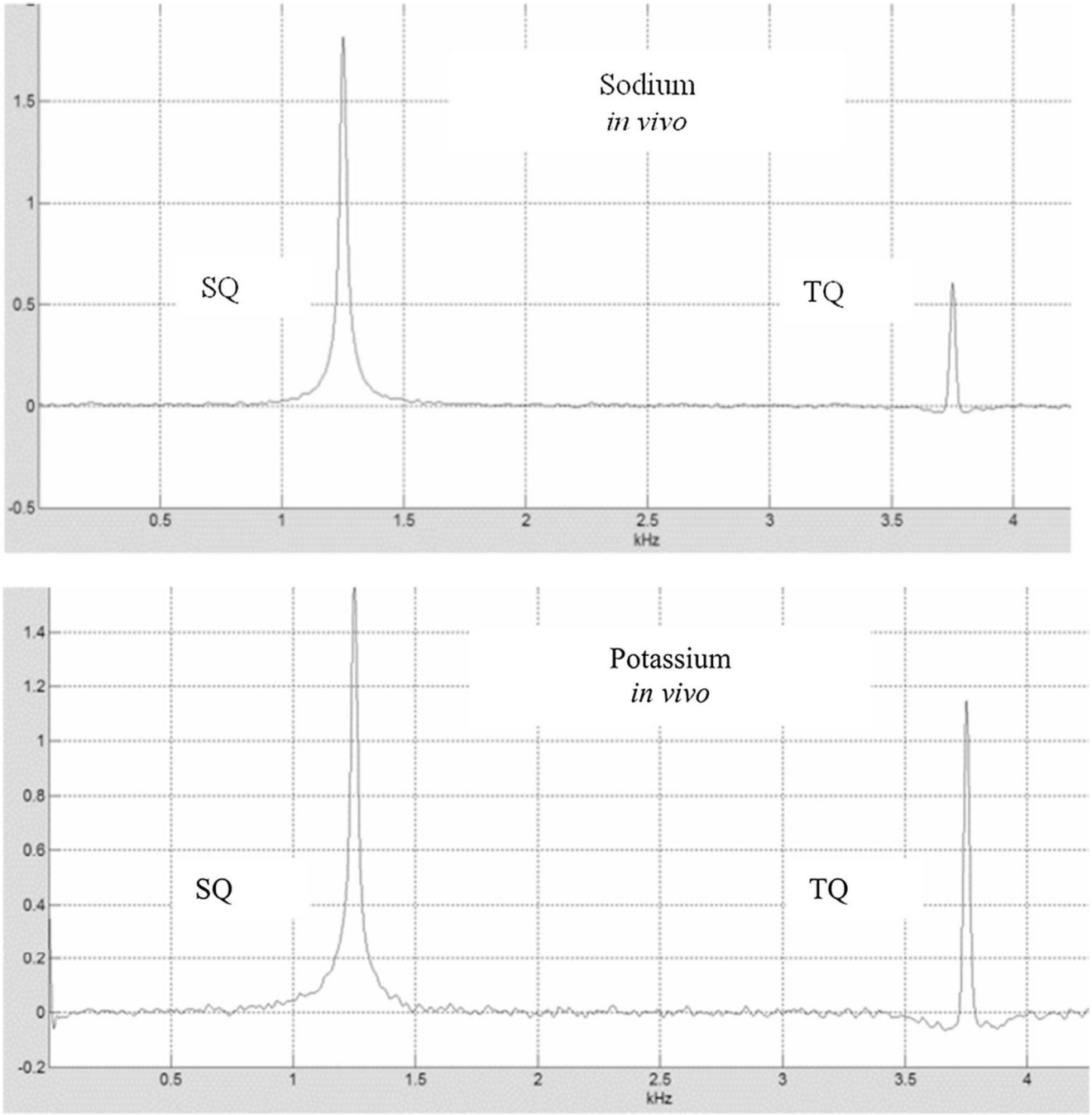

Fig. 10.

Detection of sodium and potassium in the in-vivo rodent head at 21.1 T. The two triple quantum (TQ) peaks in each spectrum represent the signal from different electric potential regions of the tissues. In the case of sodium, the TQ signal corresponds to the bound intracellular and extracellular sodium concentration. In the case of the potassium, the TQ peak arises mainly from the intracellular bound potassium. The single quantum (SQ) peaks represent the total head sodium or potassium concentrations. Each is from the TQTPPI pulse sequence [86]

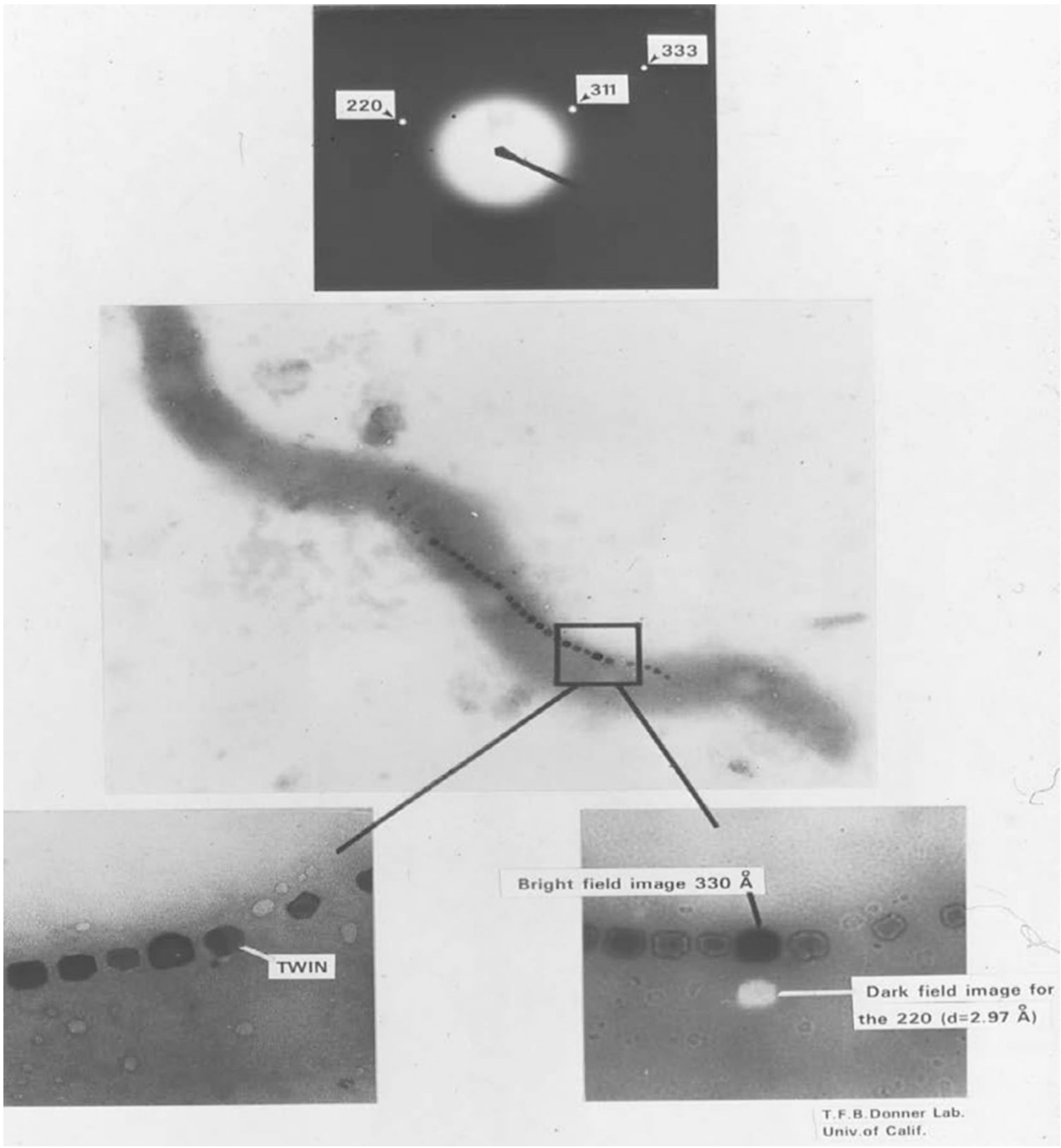

Fig. 11.

Magnetite single-domain (e.g., 50 nm) particles that are prevalent in nature also occur in the human brain with an abundance of 50 ppm. Shown here are these particles in a bacterium along with the proof that they are magnetite using a *dark-field/bright-field* displacement method to identify crystal lattice planes corresponding to those of magnetite. The displacement distance changes as a function of the magnetic lens spherical aberration coefficient, the lens current-based focus, and the specific crystal planes leading to the displacement [106]

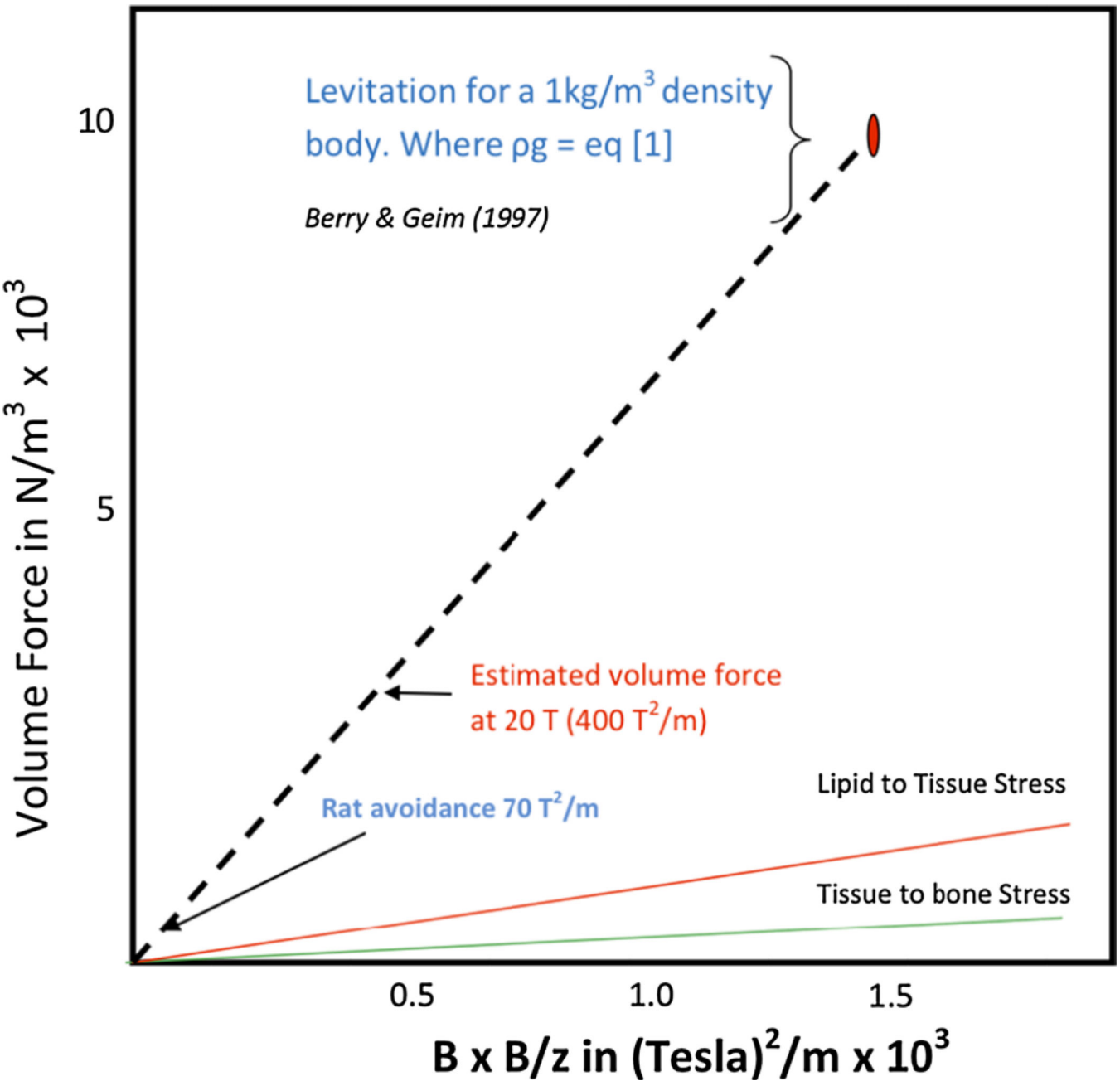

Fig. 12.

Volume force vs. magnetic field times field gradient. The force is dependent on tissue susceptibility and the product of field strength and the spatial field gradient, which is dependent on magnet design (e.g. a longer magnet will have a lower gradient)

Table 1

Low gamma nuclei available for in vivo studies are listed with average concentrations in vivo, and sensitivity relative to ^{23}Na

20 T, - in vivo MR signal/noise ratio			
Nuclei	**Frequency MHz**	**In vivo abundance mM**	**S/N ratio[a]**
Proton-1	850	94,900	1334
Sodium-23	225	50	1
Oxygen-17	115	18	1/3
Rubidium-87	278	0.6	1/6
Chlorine-35	83	38	1/10
Potassium-39	40	112	1/24
Phosphorus-31	344	10	1/37
Deuterium-2	130	11	1/97
Fluorine-19	800	0.12	1/154
Lithium-7	330	0.5	1/456
Nitrogen-15	86	0.02	1/18,500
Carbon-13	214	0.05	1/22,800

[a] ^{13}C and ^{15}N abundance based on 5 mM, ^{7}Li based on clinical levels, T_1 is included